

Case History

High-resolution quantitative seismic imaging of a strike-slip fault with small vertical offset in clay rocks from underground galleries: Experimental platform of Tournemire, France

François Bretaudeau¹, Céline Gélis², Donatienne Leparoux³, Romain Brossier⁴, Justo Cabrera², and Philippe Côte³

ABSTRACT

Imaging tectonic faults with small vertical offsets in argillites (clay rock) using geophysical methods is challenging. In the context of deep radioactive waste disposals, the presence of such faults has to be assessed because they can modify the rock-confining properties. In the Tournemire Experimental Platform (TEP, Aveyron, France), fault zones with small vertical offsets and complex shape have been identified from underground works. However, 3D high-resolution surface seismic methods have limitations in this context that led us to consider the detection and characterization of the faults directly from underground works. We investigated the potential of seismic full-waveform inversion (FWI) applied in a transmission configuration to image the clay rock medium in a horizontal plane between galleries and compared it with first-arrival traveltimes tomography (FATT). Our objective was to characterize seismic

velocities of a block of argillites crossed by a subvertical fault zone with a small vertical offset. The specific measurement configuration allowed us to neglect the influence of the galleries on the wave propagation and to simplify the problem by considering a 2D isotropic horizontal imaging domain. Our FWI scheme relied on a robust adaptation of early arrival waveform tomography. The results obtained with FATT and FWI were in accordance, and both correlated with the geologic observations from the gallery walls and boreholes. We found that even though various simplifications were done in the inversion scheme and only a part of the data was used, FWI allowed us to get higher resolution images than FATT, and it was especially less sensitive to the incomplete illumination because it also used diffracted energy. Our results highlighted the complexity of the fault zone, showing a complex interaction of the main fault system with a secondary system composed of decimetric fractures associated with the presence of water.

INTRODUCTION

Due to their confining properties, indurated argillaceous formations (clay stone) are considered as potential host media for geologic storage of high-level, long-life radioactive waste (Boisson et al., 2001) or as a geologic barrier (cap rock) for hydrocarbon trapping or CO₂ storage (IPCC, 2005). However, long-term confining proper-

ties of the clay rock layers might be affected by the presence of faults and fractures caused by past tectonic events (Bonin, 1998).

The confining properties of argillaceous rocks and the draining properties of tectonic structures are key parameters for the safety assessment of nuclear waste repositories. For this reason, the French Institute for Radioprotection and Nuclear Safety (IRSN) is conducting research programs in the argillaceous formation of the Tournemire

Manuscript received by the Editor 28 February 2013; revised manuscript received 6 June 2013; published online 21 November 2013.

¹Institut de Radioprotection et de Sûreté Nucléaire (IRSN), Fontenay-aux-Roses, and Université Joseph Fourier (ISTerre), Institut des Sciences de la Terre, Grenoble, France. E-mail: francois.bretaudeau@ujf-grenoble.fr.

²Institut de Radioprotection et de Sûreté Nucléaire (IRSN), Fontenay-aux-Roses, France. E-mail: celine.gelis@irsn.fr; justo.cabrera@irsn.fr.

³Institut Français des Sciences et Technologies des Transports, de l'Aménagement et des Réseaux (IFSTTAR), Nantes, France. E-mail: donatienne.leparoux@ifsttar.fr; philippe.cote@ifsttar.fr.

⁴Université Joseph Fourier (ISTerre), Institut des Sciences de la Terre, Grenoble, France. E-mail: romain.brossier@ujf-grenoble.fr.

© 2013 Society of Exploration Geophysicists. All rights reserved.

underground Experimental Platform (TEP, Aveyron, France) to improve its ability to assess the French storage project conducted by the French National Agency for Radioactive Waste Management (ANDRA). The Toarcian argillaceous formation of Tournemire is affected by strike-slip faults with small vertical offsets (a few meters), which are well observed in the TEP, several of them being intercepted by underground galleries and boreholes. The TEP is thus an excellent site to investigate the properties of this type of fault, taking advantage of the direct access provided by the underground works.

Three-dimensional seismic experiments are nondestructive methods that can be conducted from the surface to detect deep faults. However, these faults can be difficult to detect from the surface in argillaceous layers because their vertical displacement can be smaller than the vertical resolution of the surface seismic and because of the weak impedance variations inside the clay medium. This is the case of strike-slip faults in the TEP that have a clear expression in the clay layer under the form of various faults with small vertical displacements (a few meters at the level of the underground works). However, a 3D high-resolution surface seismic experiment could not detect them, although one was successfully detected in the deeper limestone layer, due to the higher impedance contrast and the larger vertical offset (Cabrerá, 2002). The difficulty of detecting faults in the argillaceous layer from surface seismic data leads us to consider the detection and characterization of this type of fault directly from the underground works. The use of the underground galleries thus provide a more favorable configuration, where the imaging plane crosscuts the fault plane perpendicularly. Moreover, imaging faults directly from underground works can help to determine the position and geometry of future galleries in a deep repository.

Given the large investigation distances (≈ 100 m) and the high-resolution needed (a few meters) to provide details on this kind of structure, seismic methods are well-adapted geophysical techniques. They could provide useful quantitative information about the changes in rock properties. The literature concerning seismic imaging from underground works is not abundant, and most of the work concerns the prediction of changes in rock properties when tunneling by tunnel-boring machines (TBMs), for road or rail transport. In those cases, the objectives are generally to detect, at lower cost, all kinds of geologic discontinuities (faults, joints, cavities, groundwater, abrupt changes in lithology, overpressure conditions, or depressions, etc.) located in the axis of the tunnel during its excavation and to determine their distance from the tunnel front. Those works are motivated by production and safety needs, but above all by the needs to predict rapid rock changes that may damage the TBM. For that purpose, Sattel et al. (1992) are probably the first authors to adapt the VSP processing, commonly used in oil exploration, to the tunnel configuration to get horizontal seismic profiles in the tunnel axis. This technique, known as *tunnel seismic prediction*, is now commercialized, and it has been improved and used by other authors (Inazaki et al., 1999; Ashida, 2001; Kruger et al., 2010). The experimental processes generally involve a few triaxial receivers and a higher number of explosive sources, and they allow detection of rock changes thicker than 10 m up to 100 m from the tunnel front in hard rocks such as gabbros, granites, sandstones, or pyroclastic sediments. More recently, following the example of inverse VSP of oil exploration using the drill bit as a seismic source, several authors have been interested in the use of the TBM itself as a source (Kneib et al., 2000; Ashida, 2001; Taylor

et al., 2001; Petronio and Poletto, 2002; Poletto and Petronio, 2006). With this approach, geologic changes could be detected at several hundreds of meters from the tunnel front in very hard homogeneous mica schist. Bohlen et al. (2007) and Jetschny et al. (2010, 2011) also suggest the use of very strong guided tunnel shear waves to detect structures ahead of the tunnel and to detect any rock quality changes up to 50 m from the tunnel front in gneisses, using a pneumatic impact hammer. More classical 2D seismic reflection techniques can also be used to image geologic reflectors located below or above the tunnel (Schmidt, 1959; Gendzwil and Brehm, 1993; Taylor et al., 2001). These authors are able to detect reflectors at a few tens of meters using a sledgehammer in potash mines.

The prediction of changes in rock properties in the progress of tunneling is most often constrained by poor illumination due to the existence of a single gallery. When several galleries are available, tomographic methods can be considered to characterize velocity in the area located between the galleries. Crosswell traveltime tomography has been widely used in vertical planes between boreholes for oil exploration purposes (Bregman et al., 1989), and acoustic waveform tomography has also proven its potential in this configuration (Pratt and Worthington, 1990; Song et al., 1995; Pratt and Shipp, 1999). The use of seismic tomography from underground works in other configurations is much less conventional and concerns mainly civil engineering or radioactive waste storage. A refraction and a transmission example between two galleries in limestones are presented by Cardarelli et al. (2003). In the anisotropic granitic rocks of the Grimsel underground rock laboratory, various experiments were conducted to test tomographic methods for assessing the rock quality of future radioactive waste storage facilities (Maurer and Green, 1997; Buehmann and Holliger, 1998; Albert et al., 1999; Cosma and Enescu, 2001). The authors show that even with explosive sources allowing to propagate very high-frequency energy between boreholes separated by more than 150 m, tomography images did not allow detection of all the shear zones and lamprophyres with the resolution needed. In the nuclear waste repository area of Yucca Mountain (Nevada), a large-scale tomography experiment was also performed by Gritto et al. (2004) between the top of the mountain and the 100 m depth Exploration Study Facility tunnel, to characterize subsurface faults, fracture networks, and lithologic features in the repository area (in volcanic tuff). By exploiting the arrival times of the refracted wave on the targeted layer, they could identify a high-stress area and a highly fractured zone.

Only a few seismic studies have been published about indurated clays. Most of them concern the characterization of the excavation damaged zone (EDZ) (Ramambasoa, 2001; Nicollin et al., 2008; Gelis et al., 2010; Leparoux et al., 2012). Zinszner et al. (2002) give one of the most relevant studies regarding fault characterization with seismic methods in this context. The authors provide an experimental study of anisotropy parameters at various scales in non-fractured and fractured clay rock zones of the TEP. They use laboratory measurements, sonic logs, and crosshole tomography. One can also note the numerical study that Marelli et al. (2012) propose, which deals with the acoustic and elastic waveform inversion of high-frequency borehole seismic data to monitor the bentonite plugs to be used in radioactive waste repositories in argillites and the study of Manukyan et al. (2012). To our knowledge, the only other studies concerning the underground detection and characterization of heterogeneities such as tectonic faults in clay rocks are the preliminary studies performed for the work

presented in this paper (Magnin and Côte, 2006; Breteau et al., 2010, 2011b; Magnin, 2010).

The objective of this study is to characterize the seismic velocities of a block of argillite crossed by an approximately 10-m-thick subvertical strike-slip fault zone with a small vertical offset. The properties we are interested in are the location, size, shape, and seismic velocities inside and around the fault zone and the associated fractured areas. To achieve this goal, our study is conducted in 2D in a subhorizontal plane by taking advantage of the U-shape illumination conditions provided by the underground galleries of the TEP. In particular, seismic tomography and full-waveform inversion (FWI) are performed to get velocity maps with a sufficient resolution to detect first- and potential second-order heterogeneities. In a first step, the site is presented, all the data available are compiled, and a preliminary characterization of the rock properties is done. That information is used to validate the various assumptions needed to build a numerical model of the investigated zone and plan the acquisition of a dense seismic data set. Synthetic viscoelastic data are computed in the numerical velocity model and compared with the experimental data. In the third part, we explain the two imaging techniques used: First-arrival traveltome tomography (FATT) gives a smooth velocity map, and FWI of the transmitted P-wave can be achieved using a robust norm and very little a priori information to get higher resolution velocity maps. First, the results obtained for synthetic data are presented and discussed. Then, both techniques are applied on the field data. Both results are then validated by comparison with the structural information obtained from horizontal logs and geologic observations on the wall of the galleries and in boreholes. A final structural interpretation is proposed and discussed in the last part.

GEOLOGIC SETTING AND SITE CHARACTERIZATION

The TEP is located in a Mesozoic marine basin on the Southern border of the French Central Massif. The sedimentary series in this site is characterized by a subhorizontal monoclinial structure (dip $< 5^\circ$) composed of three major layers of Jurassic age (Figure 1). The whole structure is affected to the north by a regional fault: the Cernon fault. The Tournemire argillaceous medium corresponds to a 250 m thick layer consisting of argillites and marls (Toarcian and Domerian). This argillaceous layer is located between two limestone and dolomite layers (Aalenian/Bajocian in the upper part, and Carixian/Sinemurian in the lower part) separated by two aquifers. Tectonic faults and fractures at different scales affect this monoclinial structure. The fractures are mainly developed in the limestone and dolomite series. In contrast, the argillaceous medium is affected by several faults with small vertical offsets (a few meters), which are associated with fractured zones (Bonin, 1998; Cabrera et al., 1999; Constantin, 2002).

The TEP is composed of a 1.9 km long railway tunnel that was excavated in a north–south direction more than a century ago in the Toarcian argillite layer (Figure 1). Several recent galleries have been excavated since 1996 in directions perpendicular and parallel to the

tunnel (Figure 2). Some Jurassic normal fault and strike-slip faults related to the compressional north–south to northwest–southeast-trending Pyrenean tectonics (40–50 million years ago) are intercepted in the galleries and in boreholes. The fault zone studied here is subvertical and oriented in the north–south direction (F1 in Figure 2). This is an old normal Jurassic fault reactivated during the compressional tectonics. Its vertical extent is several hundred meters, and its vertical offset is a few meters at the level of the galleries (Cabrera, 2002). The horizontal displacement is around a few tens of meters. The affected zone at the gallery WEST08 is approximately 10 m large and is characterized by fractures, fault planes,

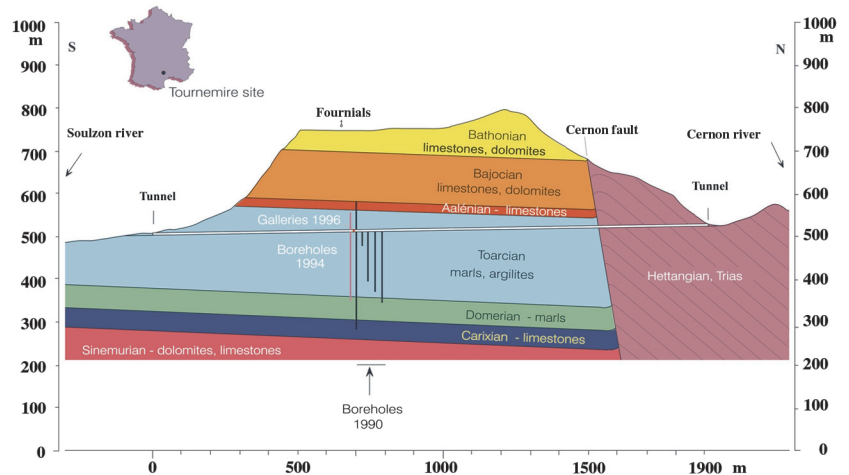


Figure 1. Geologic cross section of the Tournemire site along the tunnel of the TEP. The galleries are located in the central part of the TEP.

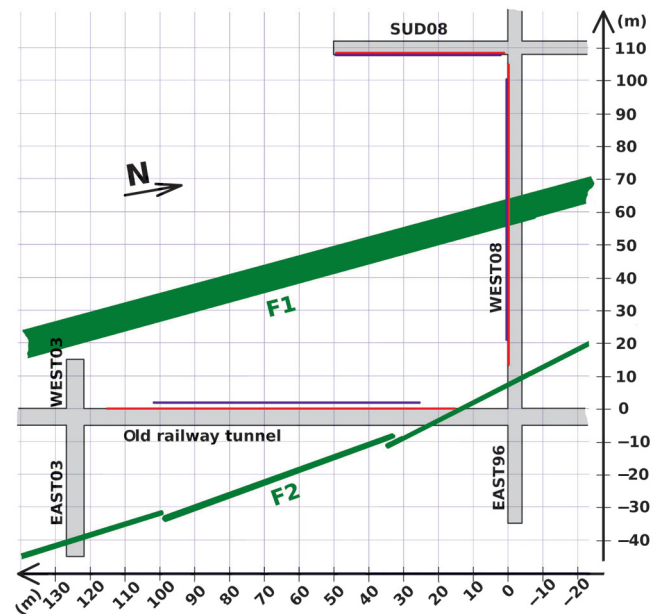


Figure 2. Map of the central zone of the TEP showing underground works and fault zones F1 and F2 at their location (green) expected from visual inspection of galleries and from information in boreholes. The positions of sources and receivers, respectively, represented in red and blue, delimit the investigated area.

and cataclastic material. The eastern side of the fault is an abrupt boundary, whereas the west side appears as a succession of undisturbed rock and fractured zones. The width of the zone with grinding material is approximately 5 m, and is concentrated on the eastern side of the fault. A second fault zone (F2 in Figure 2) with an almost similar orientation and a well-delimited cataclastic zone (≈ 1 m) with grinding material and calcite is also intercepted. The area investigated in this study is delimited by the old tunnel and the galleries WEST08, SOUTH08, and WEST03.

The particular context of the TEP implies for seismic imaging several specificities and difficulties that have to be studied before choosing an imaging technique. As shown in Figure 2, the underground configuration provides an original illumination of the target with up to three perpendicular galleries that can be used to image a subvertical structure in a subhorizontal plane. But 3D effects may have an influence and have to be considered. Furthermore, the Toarcian argillite formation is characterized by a strong vertical transverse anisotropy ($\sim 30\%$) measured by Zinszner et al. (2002).

The imaging issue in the context described above in its full complexity should require 3D viscoelastic anisotropic modeling and inversion. Because it is computationally prohibitive, especially for FWI, various simplifications have to be done. The main assumption is considering our investigated domain to be a 2D horizontal isotropic plane. The validity of the assumptions is discussed hereafter in the specific context of the TEP, taking into account the rock properties and the geometry of the galleries.

To characterize the rock outside of the fault zones, we take advantage of the presence of several long vertical boreholes crossing the investigated area and for which logs are available. Preliminary measurements were also performed in the TEP in 2009 and 2010 (Magnin, 2010) to get horizontal velocities, including high-resolution seismic refraction surveys along gallery WEST08

(crossing the fault zone) and a few records in the gallery WEST08 with shots in gallery SOUTH08. Those records led to estimating the P- and SH-wave velocities in the unfractured argillite in the horizontal direction to 3700 and 2150 m/s, respectively. Using Thomsen's anisotropic parameters determined by Zinszner et al. (2002), we were able to also infer the vertical velocity in the frequency range of interest and plot the anisotropic velocity diagrams for P-, SH- (in-plane polarization), and SV- (out-of-plane polarization) waves of Figure 3. The bedding plane is inclined about 5° to the north, and the galleries are nearly horizontal. The thick gray line in Figure 3 represents the position of the galleries relative to the bedding plane. This shows that the weak inclination of the isotropy plane relative to the imaging area does not significantly affect the velocities, resulting in errors of, respectively, 0.21%, 0.18%, and 0.36% on the P-, SH-, and SV-velocities. This allows us to consider the medium to be isotropic in the investigated domain if the 2D assumption is respected.

The vertical logs of upward and downward boreholes drilled from the tunnel indicate that at the galleries, the argillite layer can be considered homogeneous up to the Aalenian limestones located 40–50 m above, except for some decimetric limestone beds located between 36 and 45 m from the galleries. The vertical P-wave velocity in argillites is 2900 m/s. Aalenian limestones are isotropic with $V_p = 4500$ m/s. Thus, no refracted waves on limestone beds can be recorded between the galleries because the limestone layers are not located within 20 m of the galleries. Moreover, a reflection on the Aalenian layer should be recorded at 34 ms. The use of horizontal excitation in the galleries is not favorable to such vertical reflections, and the vertical transverse anisotropy is also associated with a very high attenuation anisotropy (Zhu et al., 2007). Thus, the recorded waves reflected from the Aalenian limestones and from the decimetric limestone beds are not expected to carry a significant energy. But this must be verified in the data, and removed if necessary to allow the inversion of the seismic waveforms in 2D with isotropic propagation assumption.

Because of their 3D shape, the galleries cannot be fully taken into account in the model used for 2D modeling and inversion. However, their impact on the generated and recorded waveforms can be quite significant, especially because, depending on the wavelength, waves do not interact in the same way with the gallery's free surface. For low frequencies, the wavelengths are large compared to the gallery size, thus compression waves and shear waves generated on the wall of the gallery behave as if they were propagating in an homogeneous medium (without gallery). But when the wavelengths are small compared to the gallery size, the wall of the gallery behaves as an infinite free surface, allowing propagation of Rayleigh waves. For intermediate wavelengths, Jetschny et al. (2011) show that a tunnel surface wave propagates along the gallery. This tunnel wave is dispersive with velocities varying from S-wave to Rayleigh-wave velocity when the wavelength-to-diameter ratio varies from 1.2 to 0.6. The curve in Figure 4a illustrates, following Jetschny et al. (2010), the role of the gallery as a function of the frequency in the case of TEP galleries in which the diameter is about 4 m. Following Jetschny et al. (2010), the TEP tunnel wave behaves like a body shear wave up to 500 Hz, like a Rayleigh wave above 1000 Hz, and is a dispersive tunnel wave in between.

Moreover, the galleries are surrounded by a low-velocity EDZ of 0.5 to 2 m (Magnin and Côte, 2006; Nicollin et al., 2008; Gélis et al., 2010; Leparoux et al., 2012). The EDZ is caused mainly

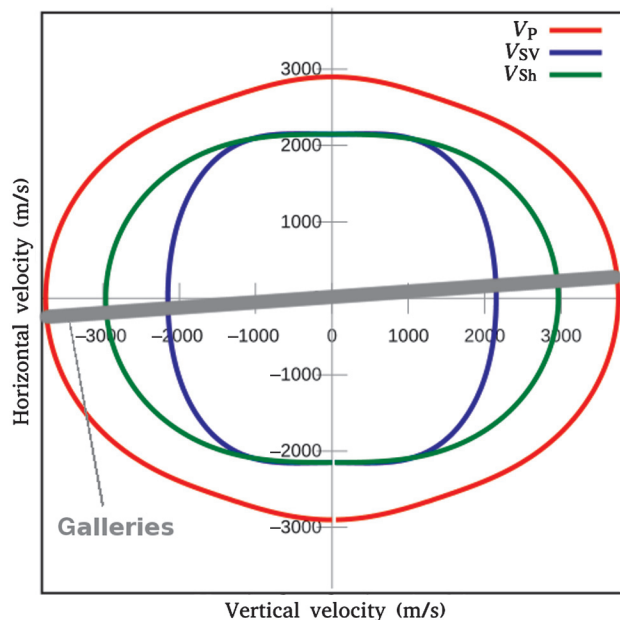


Figure 3. Anisotropy diagram computed using Thomsen's parameters (Thomsen, 1986) estimated by Zinszner et al. (2002) and velocities estimated in the preliminary studies. The thick gray line represents the relative inclination of the galleries compared to the stratification plane in the most unfavorable configuration (5°).

by unloading joints and fracturing resulting from the argillite desaturation (Matray et al., 2007; Hedan et al., 2012). This zone is characterized by lower velocities and strong wave attenuation all along the gallery walls. The radius affected depends on the drilling technique, the size, type, shape, orientation, and age of the galleries. The propagation nearby the gallery walls is thus more complicated: The frequency content is lowered by the EDZ due to strong attenuation, P-waves are refracted beyond the EDZ, and Rayleigh waves are dispersive due to the velocity gradient. This is illustrated in the dispersion diagram in Figure 4b where higher modes can be seen for frequencies higher than 500 Hz. To check the behavior of the tunnel wave in our configuration in the TEP, a 12-geophone shot gather is recorded on the wall of the gallery WEST08 for a hammer shot in gallery SOUTH08. A maximum of energy is

recorded at about 300–400 Hz, and the P- and S-waves are still energetic, respectively, up to 1500 and 1000 Hz. Those data are compared with 2D viscoelastic numerical modeling using similar sources, when the two galleries are replaced, respectively, either by absorbing boundary conditions (perfectly matched layers [PML]) or by free surfaces, using the modeling code of Brossier (2011). The results in Figure 5 show that P- and S-waves transmitted directly between the galleries are well reproduced, but the Rayleigh wave that propagates along the free surfaces of the two galleries is not recorded in the field. Those observations validate our assumption that for data recorded in transmission between galleries, the galleries would be better modeled in 2D by considering an infinite medium without galleries. For the waves generated and recorded on the same gallery wall (refracted, tunnel, and Rayleigh waves), this assumption would be valid only up to 500 Hz.

Several small-scale high-resolution refraction surveys conducted along the wall of gallery WEST08 (Magnin, 2010) gave an estimation of averaged velocities inside the fault zone ($V_P = 3350$ m/s) and in the undisturbed rock ($V_P = 3700$ m/s). The distance where lower velocities are detected is about 10 m. The velocity contrast can be represented by its reflection and transmission coefficients $R = 0.05$ (respectively, $T = 0.95$). This very low reflection coefficient means that most of the energy is transmitted and very little energy is reflected by the interface. However, the refraction survey also shows that the fault zone is composed of small high-velocity and low-velocity blocks with velocities ranging from 2600 to 3700 m/s. Furthermore, possible sparse fracturation associated with the breccia could make the interfaces smoother and could cause severe attenuation.

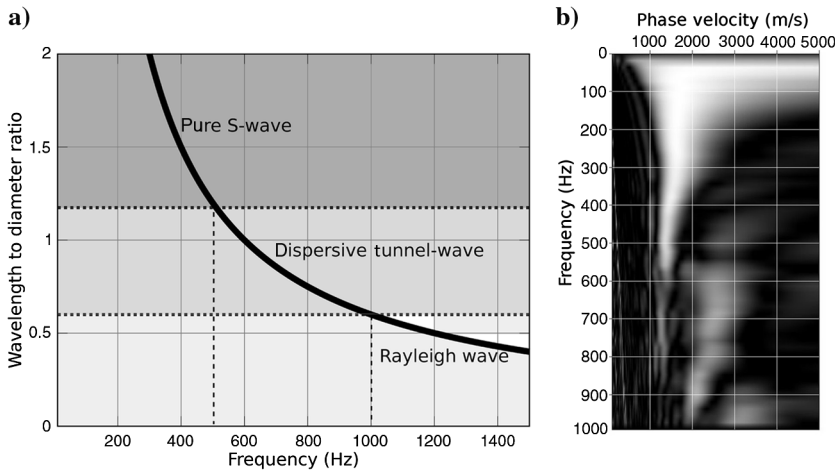


Figure 4. Impact of the gallery on shear waves propagating along the galleries. (a) Wavelengths-to-diameter ratio versus frequency and behavior limits according to Jetschny et al. (2010). (b) Rayleigh-wave dispersion diagram computed from preliminary seismic data recorded in the undisturbed rock in gallery WEST08.

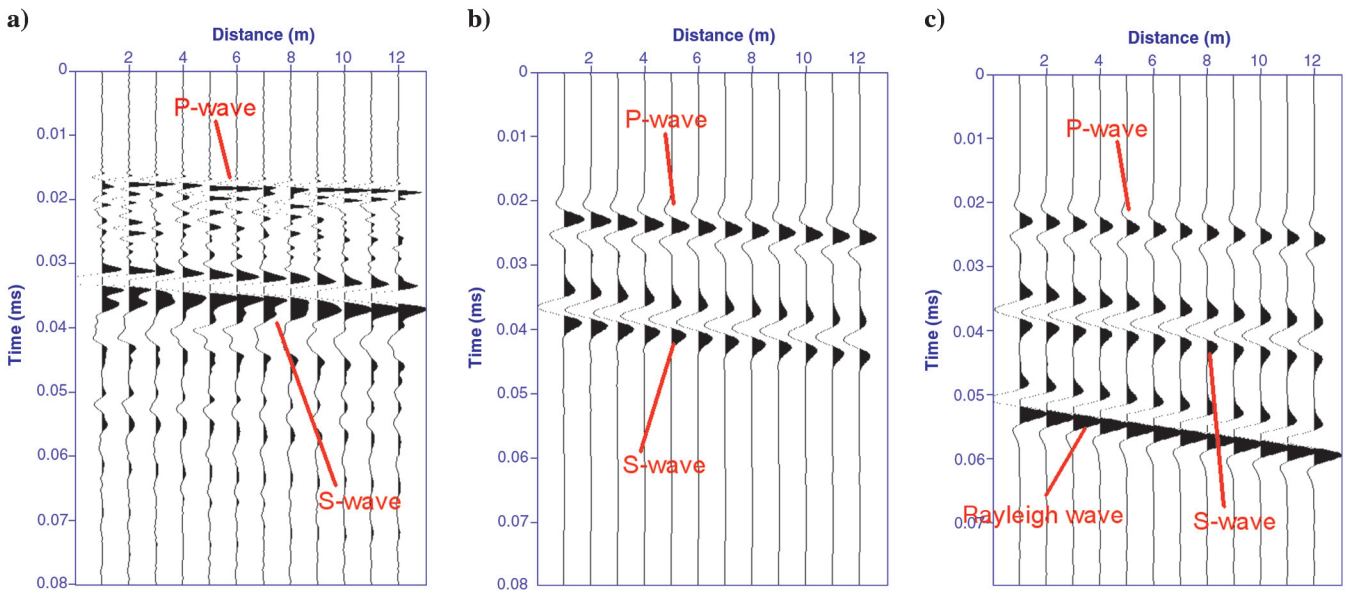


Figure 5. Effect of the galleries on shear waves: (a) experimental shot gather, (b) synthetic shot gather computed with absorbing boundary conditions, and (c) with infinite free surfaces.

In any case, the fault zone, in terms of seismic imaging, appears in this configuration to be a very unusual target: The background clay medium is supposed to be homogeneous, and the fault zone does not present itself as a blocky low-velocity area, but rather as an alternation of comminuted zones with compact undisturbed blocks or fractured regions. We expect that the footprint of the fault in the seismic data will be very complex.

Several attempts to evaluate the attenuation coefficients were performed by several methods (e.g., spectral ratio, rise time). However, none of the methods could provide accurate estimates, probably due to the presence of medium heterogeneities and to the EDZ. Finally, a coarse estimation of an effective quality factor was done by trial and error with numerical modeling. The quality factors estimated ($Q_p = 25$ and $Q_s = 15$) are lower than those suggested by Zinszner et al. (2002) ($Q_p \approx 100$).

Considering these parameters and the 2D isotropic assumption discussed above, a numerical velocity model as close as possible to the medium is constructed to better understand the complexity of the seismic wave propagation in underground works and to simultaneously perform the imaging process on synthetic data for a known medium. Numerical simulations are presented in the next section and compared to measured data.

2D FIELD DATA ACQUISITION

The acquisition layout extends over the old tunnel and the galleries WEST08 and SOUTH08, forming a U around the area of investigation (Figure 2). Ninety-six geophones were driven horizontally directly into the rock along the walls of galleries WEST08 and SOUTH08. In the tunnel, 20 more geophones were placed in 2 m boreholes to pass the tunnel masonry and the EDZ that is bigger in this area. To record the horizontal displacement and to get the low-frequency content needed for FWI (Virieux and

Operto, 2009) and the high frequencies needed to have sufficiently high resolution, 40 Hz geophones were used. The distance between the receivers was 1 m in gallery SOUTH08 and 2 m in gallery WEST08, except around the fault zone where the distance was restricted to 1 m. Twenty geophones were put in the tunnel every 4 m. The good coupling of the receivers was provided by phenyl salicylate. Data were acquired with a frequency sampling of 48 kHz for 205 shot positions distributed regularly every 1 m all along the tunnel (105 shots) and gallery SOUTH08 (50 shots), and every 2 m along gallery WEST08 (50 shots), except close to the fault zone where the distance between two sources was restricted to 1 m. The source was a sledgehammer of 3.5 kg horizontally projected on the walls. The hardness of the rock along the walls allows the hammer to provide energy from 30 Hz and up to more than 1000 Hz, with a maximum amplitude around 400 Hz. A coherent signal is recorded up to 600 Hz for the longest transmission distances between gallery SOUTH08 and the tunnel. Accurate positions of shots and geophones in 3D were recorded by a land surveyor. The complete data set thus comprises 23,780 traces, including transmission and reflection configurations.

To generate a similar synthetic data set, we built a numerical model of the investigated area and used a 2D isotropic viscoelastic frequency-domain discontinuous Galerkin finite-element modeling algorithm to simulate the propagation in this model (Brossier, 2011). The velocity model is sketched in Figure 6. The viscoelastic properties, summarized in the same figure, are based on the preliminary characterization presented previously. Density and attenuation are assumed to be constant in the whole domain. The model includes the main fault zone F1 (considered thickness 5 m) and the smaller fault zone F2 intercepted in the gallery WEST08 (thickness 1 m). The width of the fault zones is chosen to be the width of the disturbed zones with grinding material observed in gallery WEST08. The model is extended to the north to reproduce large-offset body wave reflections on the fault zone from gallery SOUTH08. Then it is extended on the four sides to include 45-m-thick PML absorbing boundary conditions (not shown in Figure 6). The model is finally discretized in triangular regular meshes with a size of 0.15 m to compute the data in the frequency range 40–1200 Hz and to avoid numerical dispersion. The sources are implemented in the code as forces oriented normally to the wall of the galleries, and the receivers give the particle velocity in the direction normal to the walls. Their exact positions in the experimental setup (given by the land surveyor) are used for the simulation. A source wavelet built from the first derivative of a Gaussian centered on 400 Hz is used for all the shot points. Sampling parameters are the same as in the field.

A shot gather recorded in the field for a shot at the extremity of gallery SOUTH08 is presented in Figure 7a, and the corresponding shot gather computed by numerical modeling is shown in Figure 7b. The direct P- and S-waves are well observed in the three galleries in the experimental data, and they are well reproduced by numerical modeling, respecting amplitudes and arrival times. However, many differences are observed. First, the shape of the wavelet is more complicated in the case of experimental data, and it differs significantly from one shot to another because of the variability of the EDZ along the gallery walls. This implies that the estimate of the source prior to the inversion of the seismic waveforms will be essential. On the receivers located in gallery SOUTH08, we can see a slight curvature of the direct P-wave indicating its refraction at the

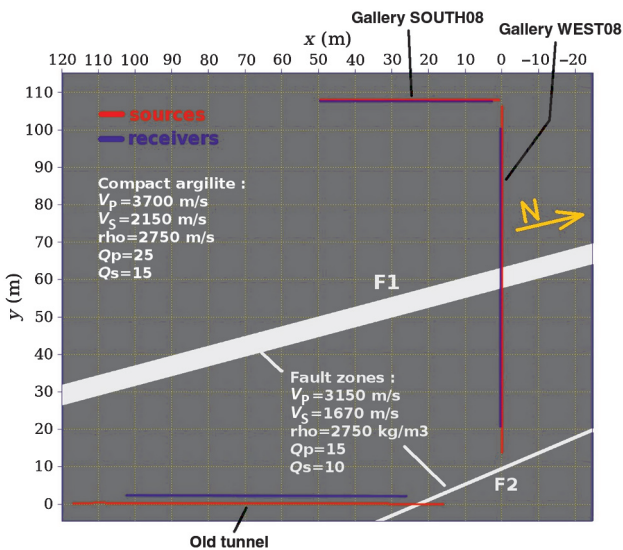


Figure 6. Velocity model of the investigated area used for numerical modeling. The model includes viscoelastic parameters of the compact argillite (black) and the F1 and F2 fault zones (white). It is extended to the north to include large-offset reflections from gallery SOUTH08, and then it extends with PML absorbing layers. Source and receiver positions along the galleries are represented in blue and red.

limits of the EDZ and the spread-out shape of the direct S-wave that suggests velocity dispersion and high-frequency attenuation. Diffractions on the galleries corners, not present in the synthetic data, are observed in the experimental data. The footprint of the fault, although very weak, is clearly visible in the synthetic data where body-wave reflections (gallery SOUTH08) and diffractions (gallery WEST08) are present. However, only a few very weak shear waves diffracted by the main fault zone nearby gallery WEST08 are visible in the experimental data set. No reflections can be identified from gallery SOUTH08. No signs of a potential reflector below or above galleries have been detected in the data, which contributes to validate the 2D assumption.

As a conclusion, the reflection configuration from a single gallery is probably inadequate for imaging the fault zones because the data seem to contain only information about the immediate vicinity of the gallery wall (i.e., dispersion, refraction, but no reflection). Moreover, we see that the waveforms recorded on the gallery where the waves are generated are highly complicated by the presence of the galleries and the EDZ, whereas the footprint of the galleries on signals recorded in transmission is not critical. Due to the difficulty to model those galleries and the poor information that can be provided by those data regarding reflected waves from the fault zone (Bretonneau et al., 2011a, 2011b), we think it is more appropriate to take into account only the signals recorded in transmission.

METHODOLOGY

To characterize the fault zone, we use two different approaches: FATT and FWI. Inversion of traveltime data is generally well constrained if the ray coverage is sufficient (existing rays in all directions). Thus, it is a quite robust technique. However, the resolution of traveltime tomography is limited by the width of the first Fresnel zone ($\sqrt{\lambda d}$ where λ is the P-wave wavelength and d is the ray length), and traveltime tomography can only provide partial information such as an average velocity in the regions where azimuthal coverage is incomplete. In our configuration, resolution of the tomography should not be better than 25 m for the largest propagation distances and 10 m for the shortest. This is not sufficient to image the details of the fault zone in all the regions of the investigated domain. Furthermore, the regions distant from gallery WEST08 suffer from an insufficient ray coverage for some azimuths, due to the three sides' incomplete illumination. Conversely, waveform inversion techniques in transmission are less sensitive to azimuthal coverage because diffractions are also used in addition to the transmission phase information used in traveltime tomography (Pratt, 1999; Shen et al., 2006; Gao et al., 2007). The directly transmitted phases provide the low wavenumbers of the velocity model, such as when using FATT. The diffractions provide higher wavenumbers and allow repartition of the diffracted energy in all the directions, thus improving the illumination of the investigated domain. Moreover, the expected resolution of FWI should improve that of FATT as it reaches its optimal resolution of $\lambda/2$ for the zero-offset reflection data set (3 m with P-waves and 1.75 m with S-waves at 600 Hz). Despite being a technique subject to intense development for the past 25 years, FWI has not yet proven its robustness in the case of complex experimental data (Virieux and Operto, 2009). Those difficulties are, among others, due to the complexity of the direct and inverse problem, to numerous approximations (2D, acoustic, no attenuation, isotropic) and to ill conditioning. However, encouraging results on experimental data

have already been presented in transmission configurations between boreholes (Pratt and Shipp, 1999). The choice of the initial velocity model is often a crucial point in waveform inversion because large wavelengths in the model are necessary to recover smaller wavelengths and because very low frequencies are generally not available for surface data at the exploration scale. Many authors use travel-time tomography to obtain the smooth initial model needed (Pratt, 1999; Pratt and Shipp, 1999). In our configuration because very low frequencies are available in the data (below 40 Hz, thus P-wave wavelengths larger than 90 m), tomography is not necessary to initiate waveform inversion. In this article, tomography and waveform inversion are not used sequentially but are used as two independent techniques to process the same data set and to compare results.

In the following section, we first describe the methods and explain how they are used in this paper. Then, both techniques are applied to a synthetic case based on our current knowledge of the medium, to evaluate the potential of each method. After that, we present how the data are prepared for inversion, followed by inversion results. Last, we compare our results with other data from geologic observations and borehole logs, and we discuss them.

FATT

The traveltimes data are inverted here using a simultaneous iterative reconstruction tomography (SIRT) algorithm (Gilbert, 1972) based on an analytical pseudoray computation. This approach is not accurate in processing refraction traveltimes, but it can very quickly handle a large number of rays, and it gives accurate tomographic images for transmission configurations with moderate velocity contrasts (Côte, 1988). Each cell of the velocity map receives a contribution from all the rays passing through a circular area of influence. The diameter of this area can be defined by a physical criterion such as the ray wavelength or the width of the first Fresnel zone. In the presented results, the diameter is fixed to 12 m. In each area, a weight is assigned to each ray to compensate for the heterogeneous azimuthal distribution of the rays. Starting from an homogeneous model with $V_p = 3700$ m/s, the solution is reconstructed

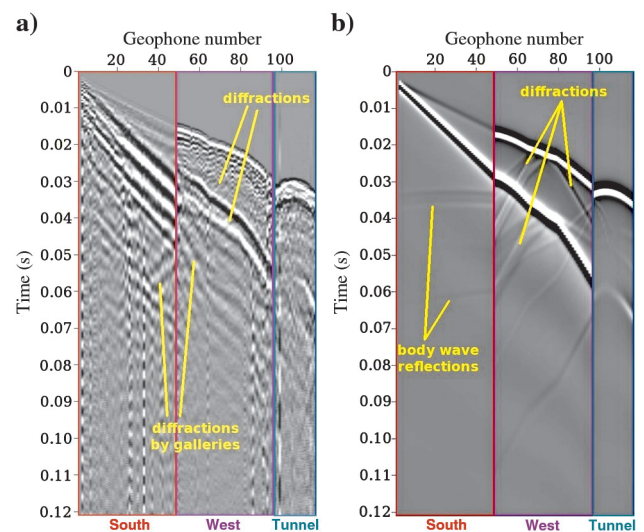


Figure 7. Synthetic and experimental shot gathers: source at the extremity of gallery SOUTH08, receivers, respectively, in gallery SOUTH08, gallery WEST08, and in the old tunnel.

iteratively until the total misfit value no longer decreases significantly (150 iterations).

To test the potential of the SIRT tomography for our problem, we first process synthetic traveltimes computed with an eikonal solver (Podvin and Lecomte, 1991) in the velocity model presented in Figure 6 with the exact source and receiver positions. The velocity map obtained after 150 iterations is represented in Figure 8b. The darkened zone represents the uncovered areas (no rays). A low-velocity zone associated to the fault zone is detected in the whole investigated domain. Near gallery WEST08 where azimuthal ray coverage is good (rays exist in most directions), the fault is imaged with a satisfying resolution and velocities inside the fault reach 50% of the true velocity perturbation. However, when one moves away from gallery WEST08, the azimuthal coverage decreases, the velocity anomaly is therefore smoothed, and the position of the fault becomes ambiguous. A triangular low-velocity area associated with the fault appears in the velocity map but does not allow the accurate location and velocity estimation of the fault zone. This kind of information corresponds to the one accessible from data recorded with the U-shape acquisition geometry.

FWI

FWI is commonly solved as a linearized least-squares problem that attempts to minimize the misfit Δd between the recorded data d_{obs} and the data $d(m)$ computed by numerical modeling in the model m (Tarantola, 1984; Pratt and Worthington, 1990; Virieux and Operto, 2009). In the frequency domain, the wave equation is a linear system and can be recast for each frequency in a compact matrix form:

$$Av = s, \quad (1)$$

where A is the sparse complex impedance matrix, vector s contains the source terms, and vector v is the monochromatic seismic wavefield that is obtained by solving this linear system.

The objective function to be minimized can be defined by

$$C(m) = \Delta d^\dagger W_d \Delta d = \Delta d^\dagger S_d^\dagger S_d \Delta d, \quad (2)$$

where S_d is a diagonal weighting operator that can be used to give a relative importance to each data and \dagger means the conjugate transpose (adjoint).

Assuming this objective function to be convex at the current frequency and in the vicinity of the current model parameter m , its

minimization using the Gauss-Newton method gives the following solution for the perturbation of the model to be estimated:

$$\delta m = H^{-1} \nabla C, \quad (3)$$

where ∇C and H are, respectively, the gradient of the objective function and the Hessian operator.

Using adjoint-state formalism (Plessix, 2006) avoids explicit computation of the Fréchet derivatives and leads to the following expression of the gradient:

$$\nabla C = \Re \left[v \frac{\partial A}{\partial m} A^{-1} \Delta d^* \right] = \Re \left[v \frac{\partial A}{\partial m} v_b \right], \quad (4)$$

where $v_b = A^{-1} \Delta d^*$ is the monochromatic wavefield obtained from the backpropagation of the data residuals Δd . The term $\partial A / \partial m$ is the so-called diffraction matrix that contains the radiation pattern of the diffractors.

The complete Hessian operator is generally too expensive to be computed. Even though recent developments have shown promising results of the truncated Newton for 2D acoustic FWI (Metivier et al., 2013) to take into account the full Hessian operator, we prefer to use the limited-memory Broyden-Fletcher-Goldfarb-Shanno algorithm, which takes advantage of information from the gradient and the gradient of the previous iterations to directly estimate the product $H^{-1} \nabla C$ without explicit computation and storage of the Hessian operator (Nocedal and Wright, 1999).

Then, the new iterate is updated with the perturbation vector δm :

$$m_{k+1} = m_k + \alpha \delta m, \quad (5)$$

where the step length α is estimated here by parabola fitting.

The waveform inversion algorithm we use is developed by Brossier (2011). The viscoacoustic or viscoelastic forward solution is computed by frequency-domain P0 discontinuous-Galerkin finite-element modeling.

Full multiparameter elastic inversion is less robust than acoustic inversion, in particular because the problem is much more nonlinear. Indeed, twice as many parameters are to be determined during the inversion process. Furthermore, it requires initial model parameters not only for V_p , density ρ , and quality factor Q_p , but also for V_s and Q_s , which are difficult to obtain with a sufficient accuracy in our context. Thus, we choose to first work with monoparameter

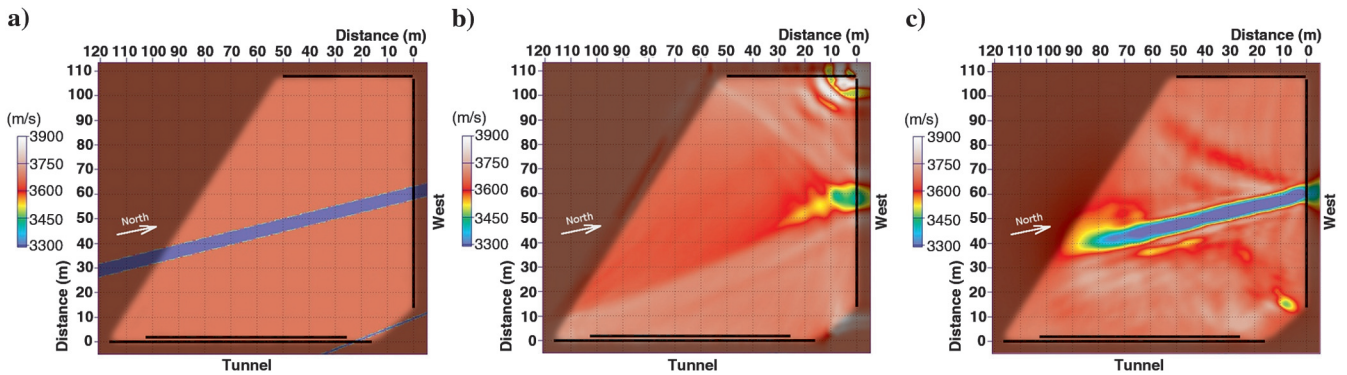


Figure 8. 2D velocity maps obtained by tomographic and waveform inversion of synthetic data: (a) exact model used to compute traveltimes and full wavefield data, (b) model obtained with FATT, and (c) model obtained with acoustic FWI.

acoustic inversion. In this scheme, Q_p and ρ are kept constant during the inversion process. However, real 3D elastic data need to be processed for supplying a data set than can be explained by the 2D acoustic forward model. For that purpose, we consider as in the tomographic case only the signals recorded in transmission and reject the signals corresponding to the source and receiver on the same gallery wall. With this data selection, and under the acoustic approximation, we focus on the first-arrival P-wave and waves arriving immediately after it. What remains in the signal is mostly due to multipath or elastic effects (slower shear waves and conversions). As [Brenders and Pratt \(2007\)](#) and [Brossier et al. \(2009\)](#) suggest, time-domain exponential damping can be applied on the seismic traces to give more weight to the first arrival and remove (or at least reduce) the influence of late shear waves arrivals in the data. In the frequency domain, this time damping is expressed as

$$\text{FT}[s(t)e^{-\gamma(t-t_0)}] = S(\omega + i\gamma)e^{\gamma t_0}, \quad (6)$$

with $S(\omega) = \text{FT}[s(t)]$ being the Fourier transform of the signal $s(t)$. Thanks to this property of the Fourier transform, such a time-domain damping is easily implemented by computing the synthetic data $d(m)$ using complex frequencies $(\omega + i\gamma)$ instead of real frequencies. The constants $e^{\gamma t_0}$, where t_0 is the beginning of the time damping for each trace, are applied to the data through the weighting vector S_d . To apply an efficient selection of the direct P-wave, t_0 is obtained from the first arrival traveltimes picking done for traveltimes tomography. Because this time-domain damping is not sufficient to completely remove shear wave signature in all the data set (especially for short offsets), S_d is completed by the empirical offset-dependent weighting function $w(x)$ represented in Figure 9a. The weighting function for a trace i is thus

$$S_{d_i} = w(x_i)e^{\gamma t_{0i}}, \quad (7)$$

with x_i being the source-receiver distance for trace i . The empirical function $w(x)$ is designed to give low importance to shortest offsets where shear waves may have an impact on any shot gathers and a decreasing importance with offset, to reduce impact of noisy large-offset data.

Because FWI is an ill-posed problem with nonunique solutions, regularization is needed to better control the inversion process and avoid getting unrealistic results. This can be done by adding a penalization term in the objective function ([Menke, 1989](#)):

$$C_p(m) = \frac{1}{2} \Delta d^\dagger W_d \Delta d + \frac{1}{2} \epsilon (m - m_{\text{prior}})^\dagger W_m (m - m_{\text{prior}}). \quad (8)$$

The weighting operator W_m is thus used to penalize solutions for bigger values of $(m - m_{\text{prior}})$. The penalization degree is adjusted by the constant ϵ and the operator W_m . By replacing m_{prior} by the local initial model, it is possible to have a selected mitigation of the impact of the gradient. The minimization of this regularized problem gives the following perturbation model:

$$\delta m = (H + \epsilon W_m)^{-1} \nabla C. \quad (9)$$

In the present paper, the model weighting operator W_m is defined by $W_m = S_m^\dagger S_m$ and allows to give a different weight to the gradient to each inverted parameter of the model. It is equivalent to using the

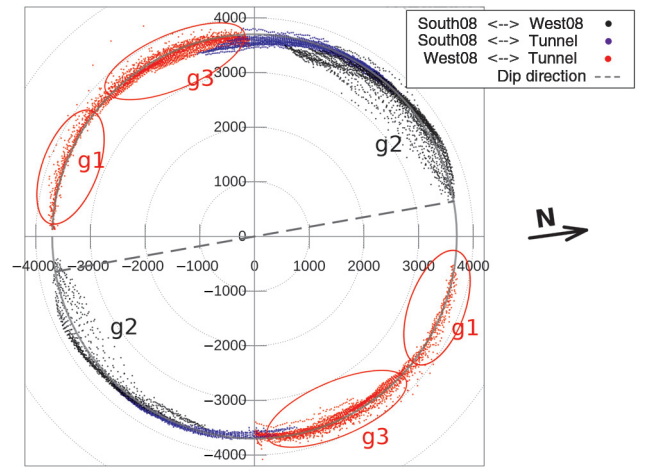


Figure 10. Representation of the average velocities for each source-receiver pair with their orientation (straight rays). Each color represents a transmission configuration (SOUTH08 \leftrightarrow WEST08, SOUTH08 \leftrightarrow TUNNEL, and WEST08 \leftrightarrow TUNNEL). Group g1 corresponds to rays that propagate in the western part of the area, in rock weakly affected, and it is associated with average velocities closed to the background velocity. In comparison, group g2 or g3 corresponds to rays passing through fault F1 and/or F2 and show much more variations on the average velocities.

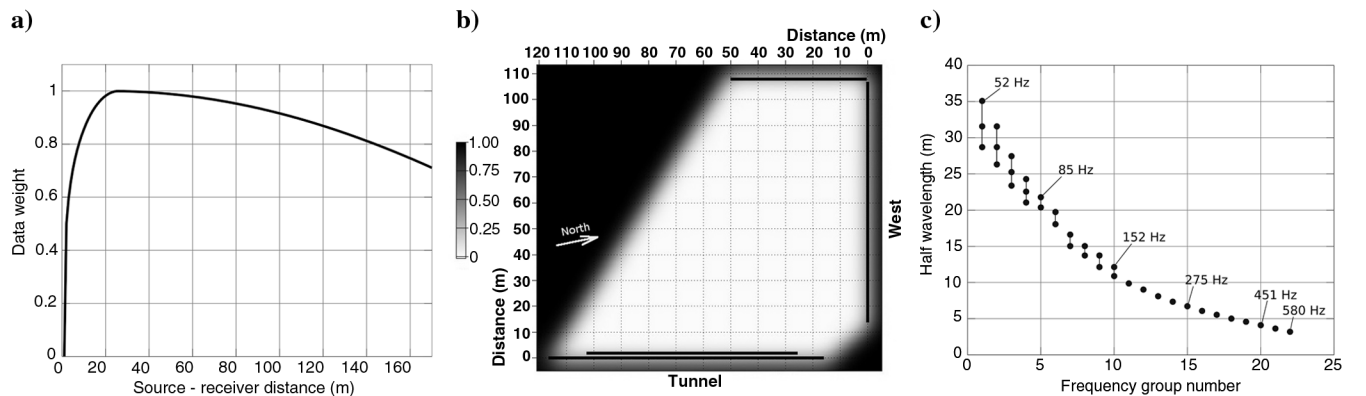


Figure 9. (a) Data weighting function $w(x)$. (b) Model weighting vector S_m . (c) Frequencies and frequency groups selected.

Levenberg-Marquardt damping coefficient, but with a different coefficient for each inverted parameter. In the test presented further in the paper, we use the weighting operator S_m represented in Figure 9b. Small constant values are used in most of the domain to regularize the inversion while giving a lot of confidence in the data, and higher values are given in areas where illumination is poor to give more weight to the initial model and avoid the appearance of artifacts. Here, W_m is also used, as in [Operto et al. \(2006\)](#), to apply a Gaussian smoothing of the gradient ∇C to regularize the inversion. The correlation length of the Gaussian

smoothing used in this work is a function of the P-wave wavelength at the local frequency, calculated with the background velocity $V_P = 3700$ m/s.

Amplitudes of the data are difficult to reproduce accurately with the modeling tool because of the inaccurate Q_P model and the 2D acoustic approximation. Because we think that in such a case, amplitude misfit could cause instability of the inversion process and may generate imaging artifacts, we define a new objective function in which all complex computed and recorded data are normalized ([Shen, 2010](#)). The data residuals are thus defined for each data i by

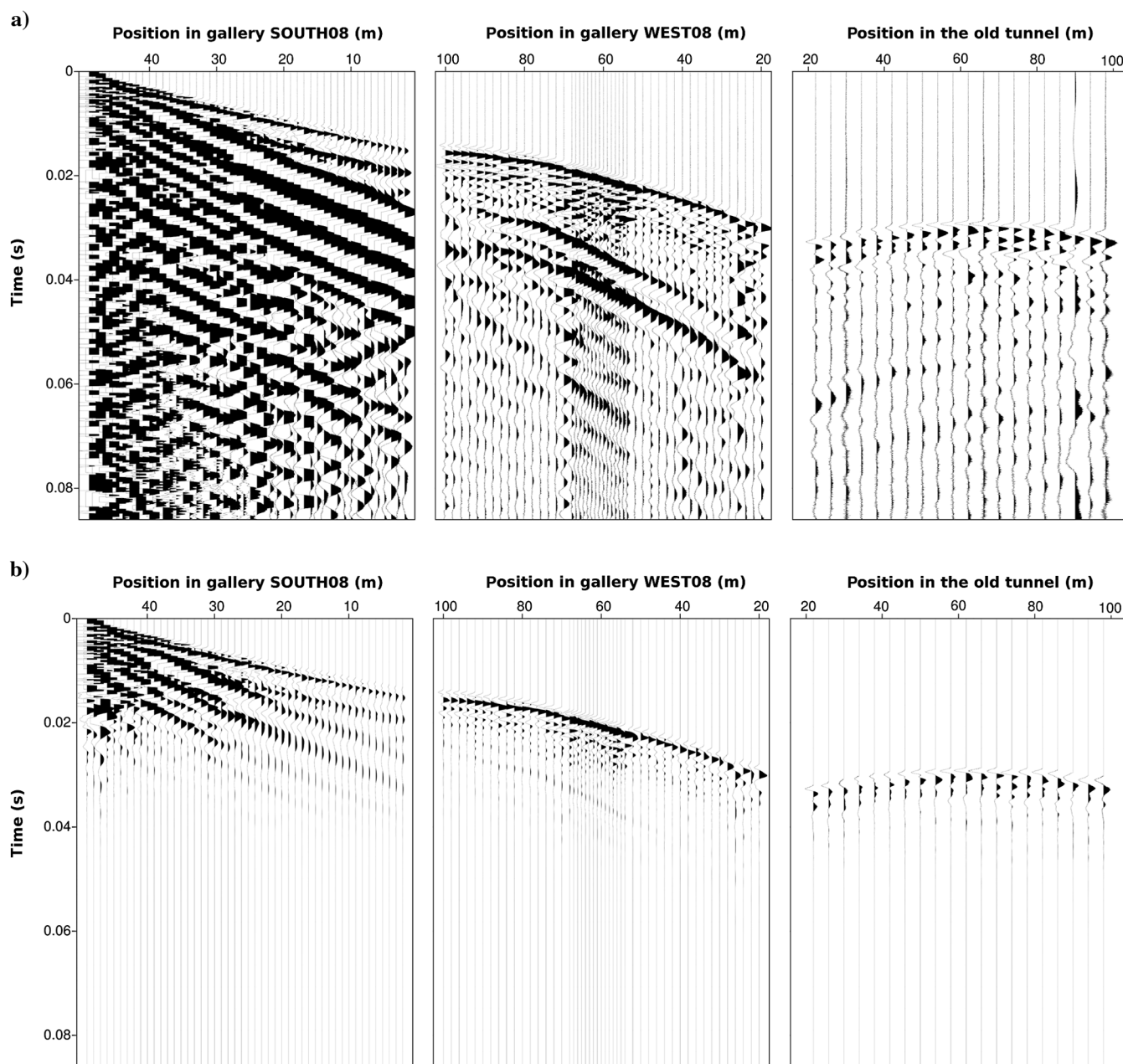


Figure 11. Examples of common-shot gathers from gallery SOUTH08: (a) Raw data and (b) data after application of the time-domain damping $e^{\gamma(t-t_0)}$.

$$\Delta d_i = \frac{d_{\text{obs}_i}}{\sqrt{d_{\text{obs}_i}^\dagger d_{\text{obs}_i}}} - \frac{d_i(m)}{\sqrt{d_i(m)^\dagger d_i(m)}}. \quad (10)$$

This new objective function is insensitive to amplitudes and minimizes only the phases of the data. Moreover, according to Shen (2010), the acoustic inversion problem recast with this new norm is more robust than classical L2 norm when applied to elastic data.

The lowest frequency for which the signal-to-noise ratio (S/N) is estimated to be good enough in the data is approximately 50 Hz. Because the investigated domain is supposed to be quite homogeneous with small contrasts, and because at this frequency the P-wave wavelengths are very large ($\lambda_P = 74$ m), starting the inversion

with an homogeneous initial velocity model with $V_P = 3700$ m/s should be sufficiently accurate to avoid cycle skipping (Sirgue and Pratt, 2004). Then, we inverse small groups of frequencies where the minimum frequency is chosen to increase so that the corresponding wavelengths decrease in each group of a constant portion (here, 12%). The frequency and associated wavelengths for each of the 22 selected frequency groups are represented in Figure 9c. The choice of the number of frequencies and the size of the groups is a compromise between robustness provided by redundancy and increasing computational times. The highest frequency inverted is 580 Hz.

At each iteration, inversion of the velocities must be preceded by the determination of each of the source wavelets to be used to compute $d(m)$. Because there is a linear relation between the

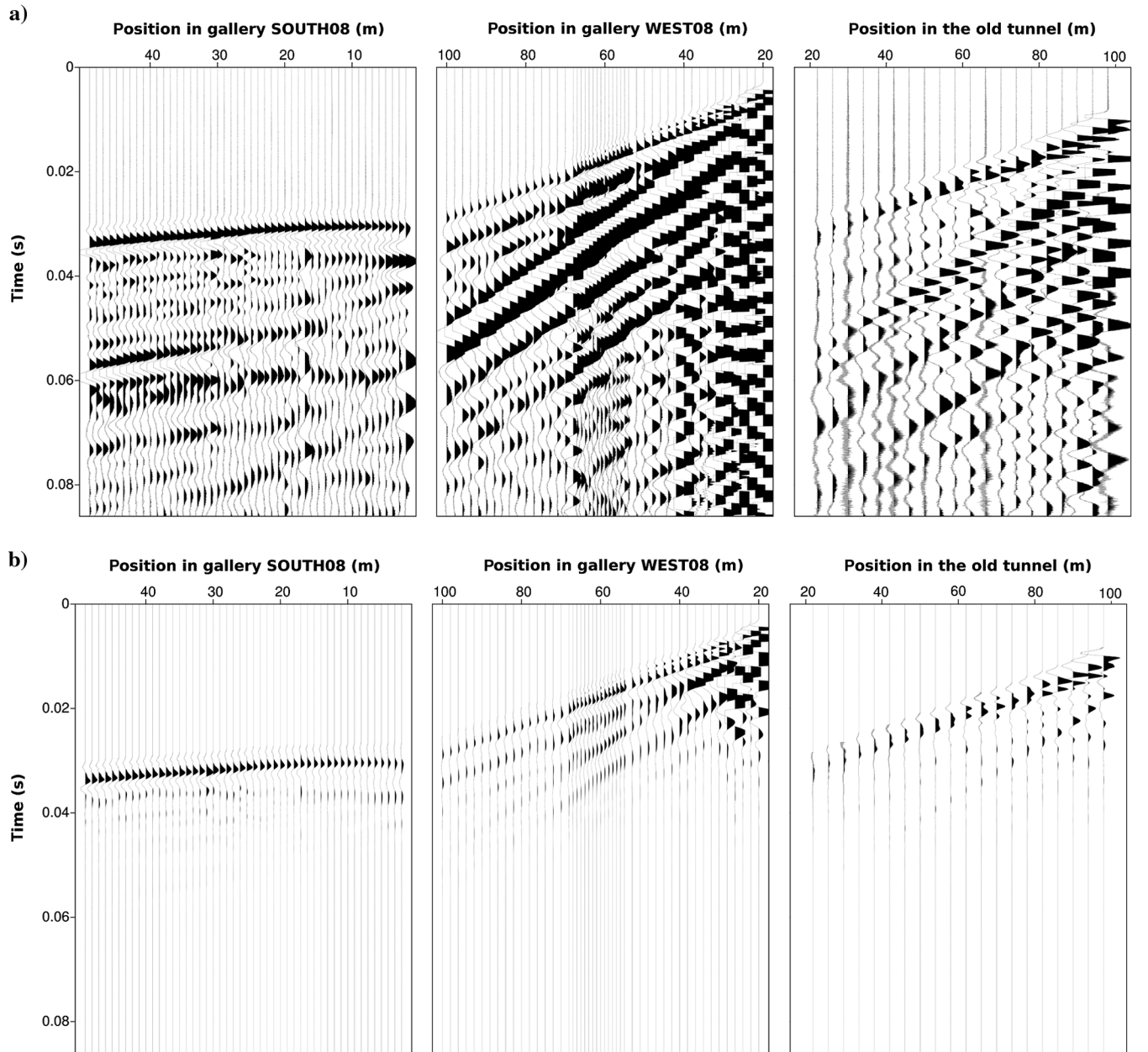


Figure 12. Examples of common-shot gathers from the old railway tunnel: (a) Raw data and (b) data after application of the time-domain damping $e^{\gamma(t-t_0)}$.

source and the wavefield, each computed shot gather can be directly multiplied by a correction term s_c obtained at each frequency by linear least-squares minimization of the misfit between observed data d_{obs} and the data computed in the current model (Pratt, 1999):

$$s_c = \frac{d(m)^\dagger d_{\text{obs}}}{d(m)^\dagger d(m)}. \quad (11)$$

Finally, because we know the velocities in the investigated domain can only be lower than the background velocity due to the presence of faults and fractures, we impose an upper limit of 3750 m/s on the inverted velocities.

As for SIRT tomography, we first apply our methodology to synthetic data computed in the velocity model presented in Figure 6 with the exact source and receiver positions. The synthetic data are computed using the same forward modeling engine as the one used for inversion, but a slightly different grid size is used, and the source wavelet as described previously (first derivative of a Gaussian centered on 400 Hz) is used. The velocity map obtained at the final frequency is represented in Figure 8c. The dark zone represents the uncovered areas, which correspond to the areas for which high values of the operator W_m are used. As expected, the image obtained with FWI shows a much higher resolution than with traveltimes tomography, and the whole fault zone is imaged with a similar resolution (even in the southern area). The velocities inside the fault zone are well estimated in the northern region of the model (90% of the true velocity perturbation), whereas this accuracy decreases in the southern region where illumination is not so good. The whole shape of the fault zone is well defined, but a few low-velocity artifacts are however present in the image.

APPLICATION TO FIELD DATA

Data preparation

The first arrival P-wave traveltimes are picked manually on the whole data set. Because the medium is fairly homogeneous and allows the transmission of seismic energy at frequencies higher than 600 Hz, the time picking did not present any major difficulties. Figure 10 displays the average velocity computed for each ray transmitted between two galleries as a function of the propagation direction in the imaging plane. This representation allows highlight-

ing of a central symmetry reflecting the reciprocity and thus the quality of the traveltimes picking. Furthermore, the concentration of data close to the 3700 m/s isovelocity circle confirms the azimuthal isotropy assumption. Finally, the variability of the velocity dispersion depending on the direction of propagation clearly indicates that some groups of rays (for instance, g1) pass through relatively homogeneous argillites, while other groups are delayed due to slower areas (g2, g3).

The amplitude of the complete field data are corrected for their 3D geometrical spreading by multiplying them by \sqrt{t} to better fit with the 2D geometrical spreading of the numerical model. Then, the $e^{\gamma(t-t_0)}$ weight is applied to each trace in the time domain, t_0 being the picked traveltimes. The signal before t_0 is set to zero to remove noise amplification caused by the exponential weight. A compromise has to be encountered for the parameter γ between an inefficient damping that leaves too strong an elastic footprint in the data and an excessive damping that leaves too little information in the data, which could lead to inaccurate results. Figures 11 and 12 show examples of common-shot gathers from two different shot positions, respectively, at the extremity of gallery SOUTH08 ($x = 50$ m) (Figure 11) and at the beginning of the old tunnel

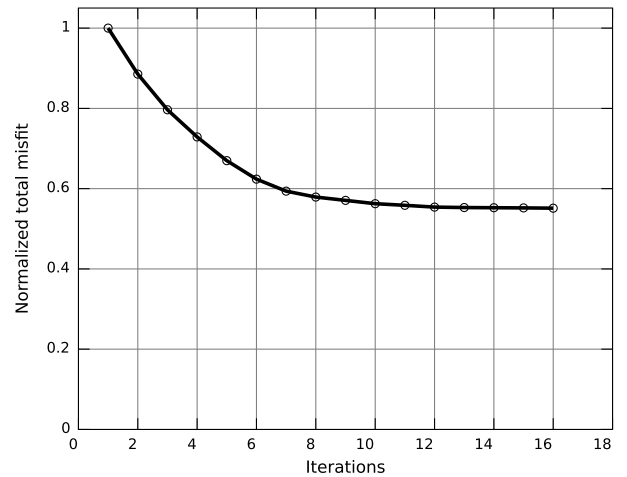


Figure 14. Decrease of the total misfit-waveform inversion of field data at the first frequency group (52–63 Hz).

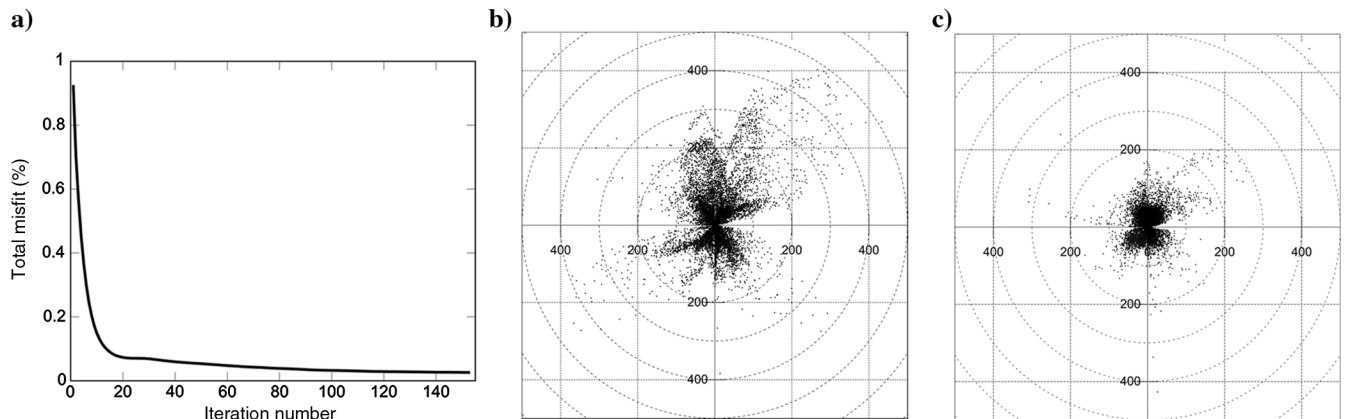


Figure 13. (a) Decrease of the total misfit, (b-c) repartition of the average velocity misfit for each ray between experimental data and data computed from the (b) homogeneous initial model and (c) model obtained after 150 iterations.

($x = 16$ m) (Figure 12), (a–c) without (c), and (d–f) with processing. This shows that the exponential damping used ($\gamma = 500$) removes most of the footprint of the direct shear waves and late arrival shear waves diffractions and mode conversions and gives a bigger relative importance to the early arrival P-wave. However, this is true only when source receiver distance is sufficiently large to separate the main direct P- and S-waves. Thus, the damping is not sufficient, for instance, when receivers and shots are on the same gallery (e.g., Figures 11a, 11d, 12c, and 12f), or when both shots and receivers are located in corners (e.g., Figure 12b and 12e). This justifies using only transmitted data jointly with the weighting function S_d of Figure 9a. The same damping is applied to the modeled data through operator S_d . This weighting is an efficient and pragmatic way to make a seismic data set more explainable by the acoustic waveform inversion tools, but it is obviously not perfect. Indeed, much acoustic information (diffractions) is also removed by the damping, and the direct P-wave that is brought out by the damping is also mixed with shear diffractions with nonnegligible amplitudes (see, e.g., the receivers located near the fault zone (60 m) in Figure 11e) that are not explainable by the acoustic inversion.

Inversion results

With both techniques, a homogeneous model with $V_p = 3700$ m/s is used as the starting model. The EDZ (< 2 m) is smaller than the wavelengths used; thus, we neglect it in a first approximation. For tomographic imaging, we proceed to 150 iterations until the total traveltimes misfit represented in Figure 13a could not decrease significantly any more. In a manner similar to the representation of the traveltimes data in Figure 10, Figure 13b and 13c illustrates the amplitude and repartition of the average velocity misfit of each ray for the homogeneous initial velocity model and for the velocity model obtained at the last iteration. The initial model gives a large distribution of the velocity misfit with some rays showing a misfit up to 500 m/s and with an average misfit of 75 m/s. In the final inverted model, the distribution of the velocity misfit is reduced in all directions to an averaged velocity misfit of 30 m/s.

For waveform inversion results, the source wavelet coefficients at each source position are first estimated for each new frequency group and at each iteration, and they are used to correct the synthetic data before computing the gradient. This allows the computed data to fit the experimental data. Because the source wavelet coefficients are estimated in a smooth homogeneous initial velocity model, they probably absorb a part of the heterogeneities of the medium close to the source positions. This might help to take into account the effect of the EDZ that is not

considered in the initial velocity model. Then, the coefficient has to be reestimated at each iteration in the updated velocity model. We present in Figure 14 the decrease of the normalized total misfit for the first frequency group (52–63 Hz). Inversion is stopped after 15 iterations because the cost function does not decrease any more. For this frequency group, the total misfit decreases significantly and stabilizes to about 60% of its initial value. This large value shows that a part of the data cannot be fully explained by the inversion. It also shows that some data are better explained by the model inverted

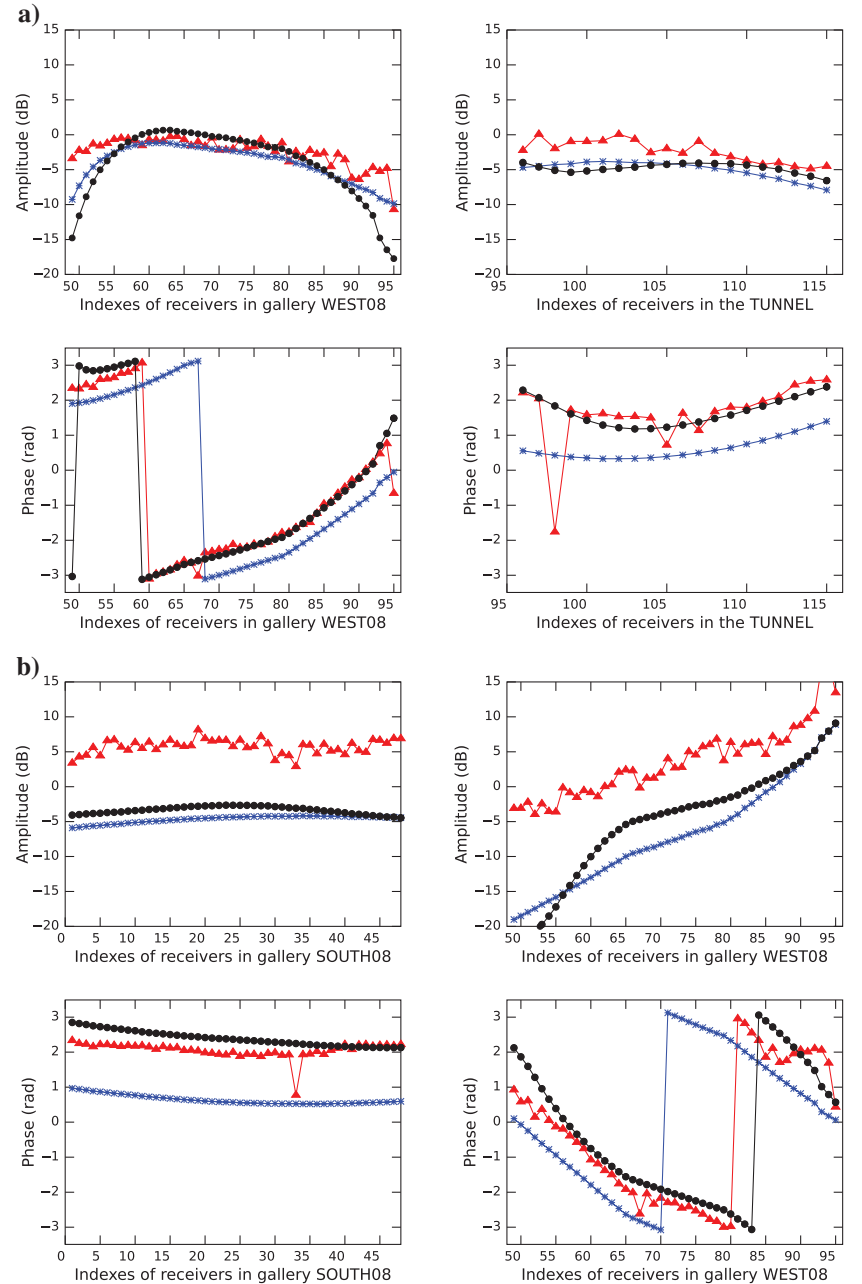


Figure 15. Phases and amplitudes at the first frequency (52 Hz) for recorded data and for data computed in the homogeneous initial model and in the model obtained at the last iteration for two shots (a) in gallery SOUTH08 ($x = 50$ m) and (b) in the old tunnel ($x = 16$ m); red \blacktriangle , recorded data; blue $*$, computed data in the initial homogeneous model; and black \bullet , computed data in the final inverted model.

than the initial homogeneous model. Figure 15 shows, for two different shot gathers, the phases and amplitudes (computed but not inverted) of recorded data and data computed in the initial homogeneous model and in the model obtained at last iteration at the first frequency of the first frequency group (52 Hz). Amplitudes are not well modeled for all the shots in the initial model, and the amplitude misfit is not reduced in the final model. Phases computed in the initial model and in the field data have a similar shape and a misfit smaller than π , which means that the source wavelet estimation is successful and that there is no cycle skipping. The phase misfit with the final inverted model clearly fits better with the experimental phases than with the initial model. However, the phase misfit is not reduced in a similar manner for all source-receiver pairs. In general, a more important misfit is observed on shots and receivers located in the corners, where diffraction on the gallery intersections cannot be well explained and where the acoustic approximation is not well respected. The final velocity model obtained with this frequency group is used as an initial model for the following frequency group, and so on, until the 20th frequency group (450 Hz). The two last frequency groups (509, 580 Hz) do not allow convergence to realistic results: This is detected because a large number of periodic anomalies appear in the images that are not consistent with the images obtained at the previous frequencies. This limitation can be explained by the lower S/N at those frequencies for some shots and by cumulative errors in the inverted velocity models at previous frequencies that lead the inversion to be stuck in a secondary minimum of the cost function.

The final reconstructed velocity maps obtained with tomography and for the last iteration of the frequency group at 450 Hz with damped robust acoustic FWI are shown in Figure 16a and 16b.

The velocity map obtained with traveltimes tomography (Figure 16a) has to be interpreted carefully because, as we showed previously on synthetic data, the east–west resolution decreases with the distance from the gallery WEST08 due to the absence of a fourth gallery and the lack of rays passing in the north–south direction. However, the resolution nearby gallery WEST08 is sufficient enough to identify some small features (a few meters). In the corner between gallery WEST08 and the tunnel, a strong low-velocity anomaly associated to fault zone F2 is detected. This anomaly has a complex shape, with different features oriented between the north direction and the N150 direction. Fault zone F1 is well detected close to gallery WEST08. Its width at gallery WEST08 is approximately 20 m, and its orientation is close to the north. Far from gallery WEST08, a low-velocity anomaly associated to

fault zone F1 is detected, but its position is not accurately known because of the low resolution in this area. Several other small low-velocity anomalies are detected, especially along the galleries (30 m along gallery SOUTH08, 90 m along gallery WEST08, and 50 and 110 m along the tunnel). Those anomalies might correspond to smaller fault or fractured zones associated to faults F1 and F2, to the EDZ, or to a combination of both.

On the velocity map obtained with FWI (Figure 16b), the strong low-velocity associated to fault F2 is also well detected. Although artifacts seem to affect the imaging in the corners where the coverage is less good, the complex shape of the fault zone F2 is also identified, highlighting several features with orientations ranging between north and N150. Because it also uses diffractions, the FWI is less sensitive to illumination than traveltimes tomography; thus, fault F1 can be imaged in a wider area than with tomography, and with a better resolution. Fault zone F1 is imaged at its expected position and orientation nearby gallery WEST08. Its width is about 20 m. However, the anomaly disappears at more than 50 m from gallery WEST08, which is not in agreement with a continuous geologic fault. More low-velocity elongated anomalies oriented between N and N140 are also clearly detected between the tunnel and the position of fault F1. Several of the small anomalies detected along the galleries with traveltimes tomography are also detected (50 and 100–110 m along the tunnel and 90 m along gallery WEST08). Finally, a complex shape anomaly is detected between gallery SOUTH08 and fault zone F1. This anomaly also suggests the presence of a structure oriented close to the N140 direction.

VALIDATION, DISCUSSION, AND INTERPRETATION

Both velocity maps obtained with traveltimes tomography and FWI show several common features. In both results, fault zone F2 appears to have the most important impact on P-wave velocity. Fault zone F1 is at its expected position at least up to 50 m from gallery WEST08, and its width is approximately 20 m. Several small features are also detected at the same positions with both techniques. But the most important information confirmed by both techniques is the evidence of the coexistence and interaction of two fault systems with orientations, respectively, to the north and N130–150. However, the magnitudes of the anomalies differ in the two results, and some detected anomalies that are not confirmed by the two images could be imaging artifacts.

To validate the imaging results and to assess the performance of the two quantitative imaging approaches used in this study, a detailed mapping of the structures that can be observed in (and around) the investigated area was performed (J. Cabrera, personal communication, 2013). This information comes from direct field observations performed during the past 10 years on the walls and the ground of the galleries during their excavation and from boreholes crossing the area. Several boreholes (4 to 16 m) were also drilled at some specific locations to validate and discuss the velocity maps obtained with the two methods presented previously. The structure mapping and the borehole locations are presented in Figure 17a and 17b, superimposed on the zone of the velocity maps that can be interpreted.

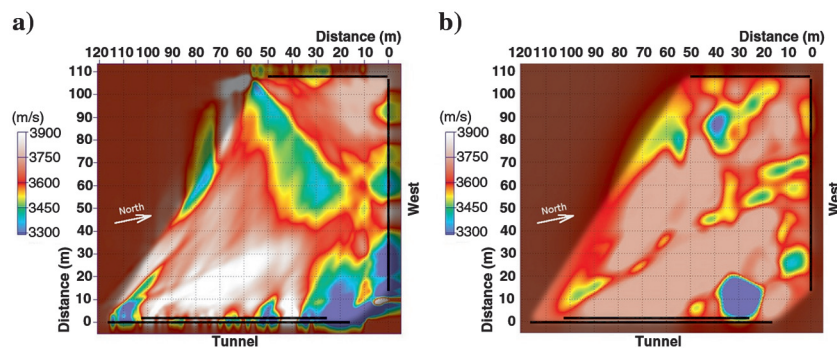


Figure 16. Velocity maps obtained from the experimental data with (a) traveltimes tomography and (b) damped robust acoustic FWI.

Moreover, a high-resolution refraction survey was performed all along gallery WEST08 using the seismic data generated and recorded along this gallery as described above. The velocity profile behind the EDZ (~1.5 m from the wall) was extracted using the plus-minus technique and median filtering. The refraction profile is displayed in Figure 18 with the corresponding profiles extracted from the traveltime and FWI velocity maps and the theoretical profile designed from the a priori geologic knowledge (position of the cataclastic zones associated to F1 and F2). The structure mapping along gallery WEST08 is also presented in the same figure.

Both P-wave velocity models, obtained with tomography and FWI, are in good accordance with the fault and fracture positions identified by the structure mapping of J. Cabrera (personal communication, 2013) in Figure 17. Most of the events identified in the structure map are detected by the imaging processes: Fault zone F1 oriented in the north–south direction, fault zone F2 with independent structures oriented from the north–south to the N140 direction and several small features located nearby the galleries. Even the small anomalies oriented N140 detected with FWI between fault F1 and the tunnel and between fault F1 and gallery SOUTH08 seems to correspond to existing small fractured zones (width of several tenths of centimeters) observed in boreholes. Velocity maps and the structure mapping together agree to show the complexity of the studied area and to show that this complexity is related to the interaction between two fault systems, oriented north–south and N140, respectively. We can also note that the width and shape of the different structures can vary considerably from one point to another over relatively short distances. On the velocity profiles along the gallery WEST08 (Figure 18), we see that all curves are consistent. The refraction profile is the most accurate because it provides a high-resolution local estimate. The profile obtained with tomography is smoother due to the low resolution, and the profile obtained with FWI have a higher resolution, but the velocity estimations are less accurate. The underestimation of the magnitude of velocity anomalies with FWI of real data was already observed by [Bretaudeau et al. \(2013\)](#). It can be associated with the presence of noise in the data. However, all profiles agree with the structure mapping along the gallery. In particular, we see that the most pronounced velocity anomaly match at the intersection of the eastern fault plane of F1 where it consists of grinding material and of a small strike-slip fault oriented N140. At this point, velocity reaches locally 3100 m/s, which corresponds to a contrast of 16% against the undisturbed rock.

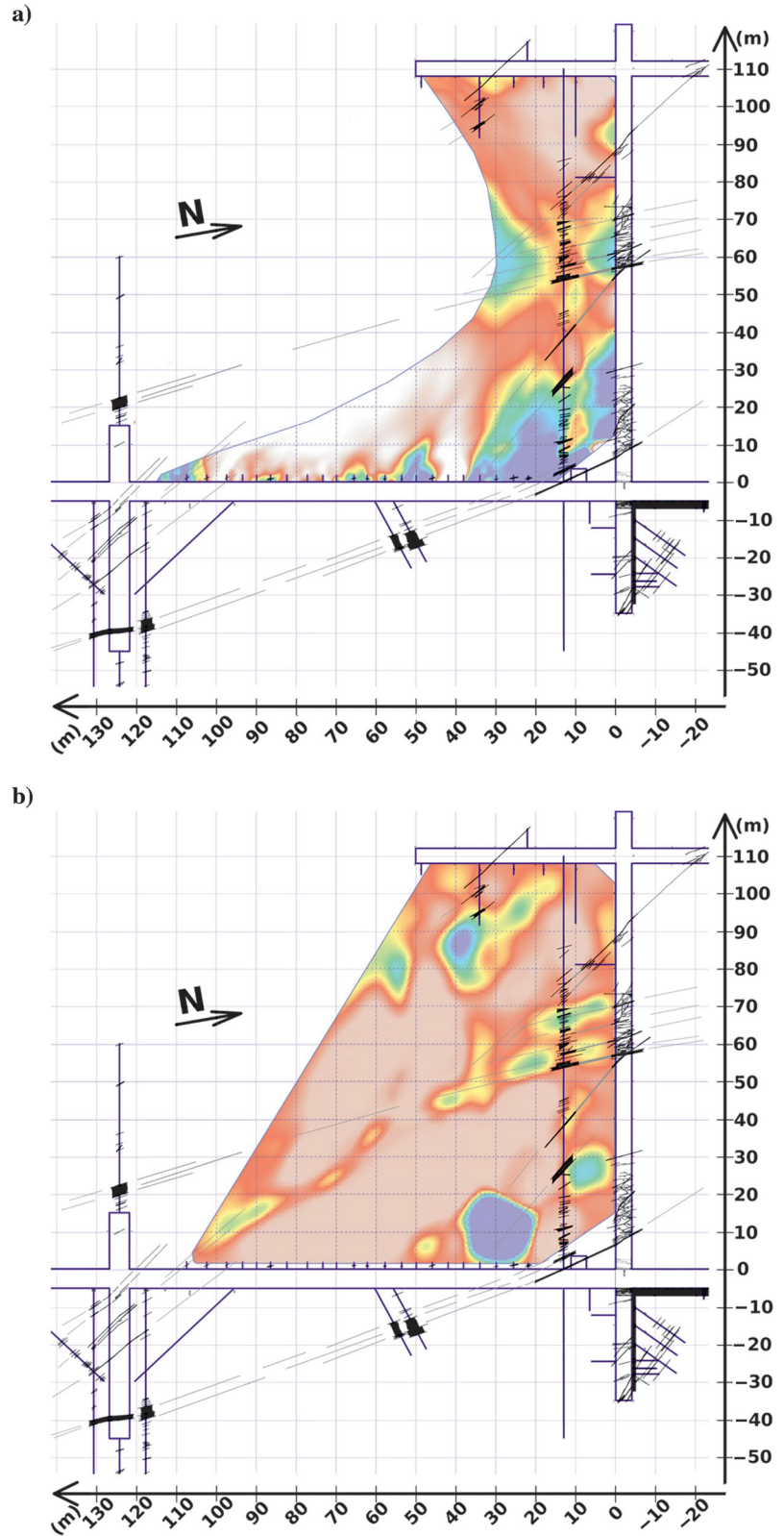


Figure 17. Velocity maps obtained from the experimental data with (a) traveltime tomography and (b) damped robust acoustic FWI, both presented with the location of fault zones and fractured areas (black) mapped from observations in galleries and boreholes (blue), (J. Cabrera, personal communication, 2013). Gray lines give locations of faults and fracture locations extrapolated from the real observed structures.

Geophysical results and direct observations are in agreement and show that the main north–south fault system is partially intersected by another fault system oriented N140. Fault F1, which was initially a normal fault, was reactivated in the strike-slip during the Pyrenean compression. During this tectonic phase, other structures such as F2, which is a pure strike-slip fault, were also created. Secondary structures oriented N140 that intersected the north–south fault system were also created. The formation of the N140 fault system can be interpreted as a consequence of changes of the stress field orientation. Those faults could have segmented and displaced pieces of the north–south fault zone studied here. We observe that the position of the N140 structures is correlated to the most pronounced velocity anomalies detected, especially if we consider their small size (submetric or metric widths). This is consistent with some direct observations that revealed that the N140 fault system is characterized by small openings along the fault planes, giving rise to the presence of water coming from the upper aquifer located in the

Aalenian limestones (Figure 1) (Beaucaire et al., 2008; J. Cabrera, personal communication, 2013).

Because the available boreholes do not cover some zones of the investigated domain, we cannot be certain of the validity of some of the detected anomalies. We know that some of the assumptions we made for FWI (for instance acoustic approximation) are not fully respected. Thus, we propose an additional test to assess what our FWI process can really image, considering the complexity of the studied area. For that, a complex P-wave velocity model is built, based on the geologic interpretation of the structural mapping, the velocity maps obtained with FWI and tomography, and the velocity estimations given by the refraction survey. An S-wave velocity model is derived from the P-wave model using a constant Poisson ratio. The complex interpreted P-wave velocity model is presented in Figure 19a. It includes the strike-slip fault system F1 and F2 oriented to the north that have been partially segmented and displaced by a posterior tectonic fault motion related to the N140 strike-slip fault system. The eastern side of the fault F1 is sharper than the western side (e.g., refraction profiles and direct observations). Note the presence of a small fault oriented N140 between F1 and gallery SOUTH08. We use this interpreted model to generate a complete synthetic viscoelastic data set and a complete pseudo-viscoacoustic data set ($V_s = 0, Q_s = \infty$) using the same modeling code (Brossier, 2011). The true experimental source and receiver positions are used. The quality factor and density are kept constant in the model. Then our robust acoustic FWI process is applied on viscoacoustic and viscoelastic data sets. The time-domain damping and the data weight designed to remove shear-waves influence from the data are kept in the inversion process with both data sets. For comparison, the final result of the acoustic inversion of the acoustic data set is presented in Figure 19b, and the result of the acoustic inversion of the elastic data set is shown in Figure 19c. Almost all the structures are imaged with a satisfying resolution when the acoustic approximation is respected, except in the tunnel-WEST08 corner where illumination is not good. However, when shear events are present and the acoustic approximation is not perfectly respected, we show that the structures are imaged with a much lower resolution. Although the main structures are detected at their expected position, the velocity map is affected by a lot of artifacts; thus, the final image is distorted. For instance, a large anomaly is detected along gallery SOUTH08 instead of the small N140 faults located between F1 and gallery SOUTH08. In a similar manner, the north–south and N140 faults in the southeast corner of

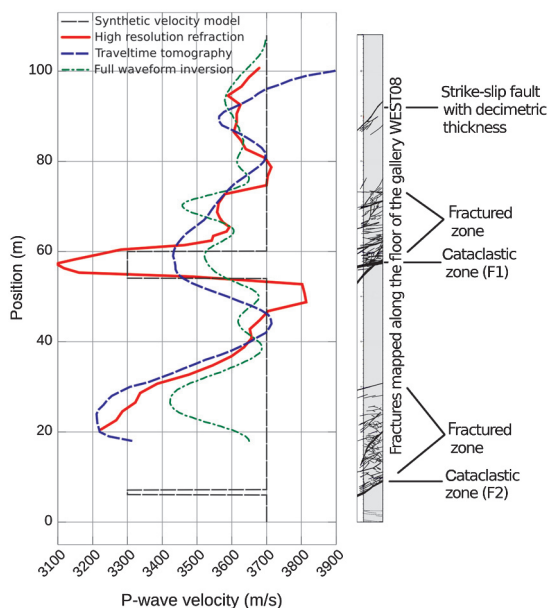


Figure 18. Fracture mapping and velocity profiles along gallery WEST08 (1 m from the gallery) from tomography and FWI compared to the high-resolution velocity profile obtained with seismic refraction.

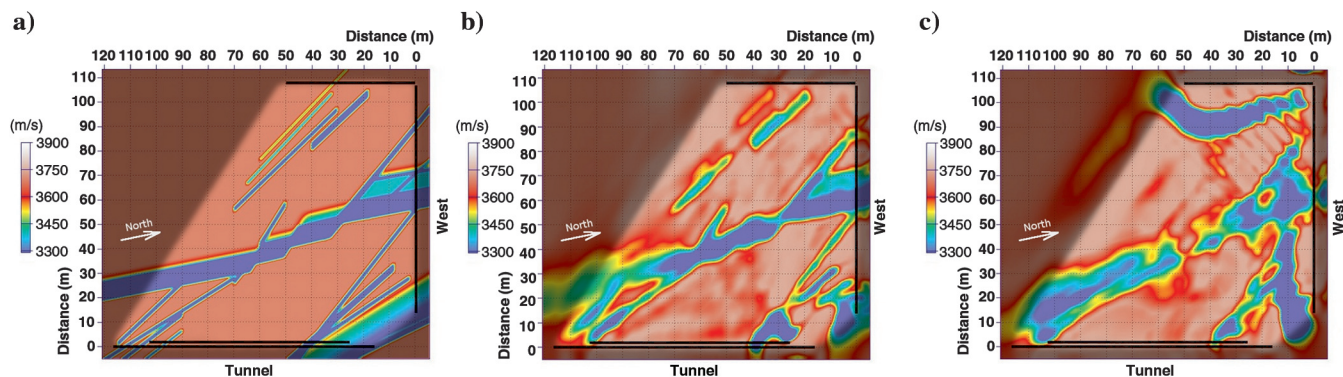


Figure 19. Velocity maps obtained in the synthetic interpreted model: (a) exact interpreted model and the final inverted models at 600 Hz from (b) damped acoustic inversion of acoustic data and (c) damped acoustic inversion of elastic data.

the images are all well separated when acoustic approximation is respected (Figure 19b), but they interfere and cannot be dissociated when the acoustic approximation is violated. That could explain why fault zone F1 disappears in this region in the image obtained on real data (Figure 16b), or the presence of some unexplained anomalies. Some similar observations on synthetic data were reported by Marelli et al. (2012) in the case of cross-borehole experiments. This test highlights the importance of the shear-wave diffractions in the data that are not completely removed by the time-domain damping, and that the inversion algorithm try to explain as P-wave diffractions. That means the solution to obtain more accurate results would be to process the elastic data using multiparameter elastic waveform inversion. Moreover, elastic inversion could give extra information on V_P and V_S , which could be interesting because the V_P/V_S ratio should be more sensitive to the changes in rock quality (as we have inside the fault zones) or to the presence of water. However, elastic inversion is more complex to apply because the problem is more nonlinear and twice more parameters have to be determined. A smooth V_S initial model could be inferred with the strategy used in this paper, but by windowing the transmitted shear wave instead of the P-wave. We also think recent developments like those proposed by Metivier et al. (2013) to take into account the full Hessian in the inversion would be very useful to properly scale the various components of the gradient of the cost function, which is a critical point for multiparameter FWI. Constraints and cross constraints could also be applied to force V_P and V_S to remain consistent.

CONCLUSION

We assessed the potential of quantitative seismic imaging techniques to detect and characterize strike-slip faults with small vertical offsets in clay-rock directly from underground works, in 2D in transmission between several galleries. FATT and a robust adaptation of FWI were tested. Both techniques provide comparable results that are both in good accordance with the direct field observations. Traveltime tomography provides accurate results with a satisfying resolution close to the gallery, but is very sensitive to the illumination (ray coverage), and thus it fails when a limited measurement configuration have to be used. The FWI process proposed here is based on a pseudoacoustic approximation and involves data weighting and time-domain damping to remove the shear-wave footprint from the data and apply successfully monoparameter V_P FWI. Amplitudes, which are not accurately modeled, are not considered in the inversion process, thus only phases of the data are used. As expected, FWI provides velocity maps with a higher resolution than traveltime tomography. Furthermore, FWI is less sensitive to the ray coverage because it uses the whole waveforms. Thus FWI provides more information than traveltime tomography. However, we show that the FWI result is affected by artifacts due to the acoustic approximation that is not perfectly adapted to those data. The use of a full elastic waveform inversion process could help to solve this limitation and provide more accurate results.

This study also yielded very detailed information on this specific fault zone. We showed the complexity of the fracturation of the argillaceous rock in this regional tectonic context. In particular, the study highlights the complex interaction of several systems of strike-slip faults having slipped at different times, and we show the footprint of the different structures on seismic velocities. Our results also tend to show that a secondary fault system oriented

N140 and with small fractured zones (inframetric to metric width) can generate relatively high velocity anomalies compared to a larger fault zone (plurimetric width). Those results are consistent with some direct observations because water coming from the upper aquifer was detected in the N140 secondary fault system that shows the high-velocity anomalies.

However, some structures detected by the seismic imaging techniques remain difficult to validate because they are quite far from the galleries and the images are affected by artifacts. Additional long boreholes should provide the necessary information to validate the central part of the investigated area.

ACKNOWLEDGMENTS

The authors would like to thank O. Magnin (TERRASEIS), O. Durand and A. Luczak (IFSTTAR), P. Desveaux (Entreprise Martinez), and E. Vi Nhu Ba (IRSN/Mines Paristech) for discussions and for their participation to the seismic experiments. This work was granted access to the HPC resources of CINES under the allocation 2012-c2012046837 made by the Grand Equipement National de Calcul Intensif.

REFERENCES

- Albert, W., J. Buehmann, K. Holliger, H. Maurer, R. Pratt, and I. Stekl, 1999, Further development of seismic tomography — Grimsel Test Site: Technical report 97-05, National Cooperative for the Disposal of Radioactive Waste (NAGRA).
- Ashida, Y., 2001, Seismic imaging ahead of a tunnel face with three-component geophones: International Journal of Rock Mechanics and Mining Sciences, **38**, 823–831, doi: [10.1016/S1365-1609\(01\)00047-8](https://doi.org/10.1016/S1365-1609(01)00047-8).
- Beaucaire, C., J.-L. Michelot, S. Savoye, and J. Cabrera, 2008, Groundwater characterisation and modelling of water-rock interaction in an argillaceous formation (Tournemire, France): Applied Geochemistry, **23**, 2182–2197, doi: [10.1016/j.apgeochem.2008.03.003](https://doi.org/10.1016/j.apgeochem.2008.03.003).
- Bohlen, T., U. Lorang, W. Rabbel, C. Muller, R. Giese, S. Luth, and S. Jetschny, 2007, Rayleigh-to-shear wave conversion at the tunnel face — From 3D-FD modeling to ahead-of-drill exploration: Geophysics, **72**, no. 6, T67–T79, doi: [10.1190/1.2785978](https://doi.org/10.1190/1.2785978).
- Boisson, J., L. Bertrand, J. Heitz, and Y. Golvan, 2001, In-situ and laboratory investigations of fluid flow through an argillaceous formation at different scales of space and time, Tournemire tunnel, Southern France: Hydrogeology Journal, **9**, 108–123, doi: [10.1007/s10040000119](https://doi.org/10.1007/s10040000119).
- Bonin, B., 1998, Deep geological disposal in argillaceous formations: Studies at the Tournemire test site: Journal of Contaminant Hydrology, **35**, 315–330, doi: [10.1016/S0169-7722\(98\)00132-6](https://doi.org/10.1016/S0169-7722(98)00132-6).
- Bregman, N., R. Bailey, and C. Chapman, 1989, Crosshole seismic tomography: Geophysics, **54**, 200–215, doi: [10.1190/1.1442644](https://doi.org/10.1190/1.1442644).
- Brenders, A., and R. Pratt, 2007, Full waveform tomography for lithospheric imaging: Results from a blind test in a realistic crustal model: Geophysical Journal International, **168**, 133–151, doi: [10.1111/j.1365-246X.2006.03156.x](https://doi.org/10.1111/j.1365-246X.2006.03156.x).
- Bretaudeau, F., R. Brossier, D. Leparoux, O. Abraham, and J. Virieux, 2013, 2D elastic full-waveform inversion of the near-surface: Application to synthetic and physical modeling data sets: Near Surface Geophysics, **11**, 307–316, doi: [10.3997/1873-0604.2012067](https://doi.org/10.3997/1873-0604.2012067).
- Bretaudeau, F., C. Gélis, J. Cabrera, D. Leparoux, and P. Côte, 2011a, Feasibility study of strike-slip faults imaging by seismic methods from underground galleries in the experimental station of Tournemire, France: Presented at 16th European Meeting of Environmental and Engineering Geophysics.
- Bretaudeau, F., C. Gélis, J. Cabrera, D. Leparoux, and P. Côte, 2011b, Strike-slip faults imaging from galleries with seismic waveform imaging methods: Presented at AGU Fall Meeting.
- Bretaudeau, F., D. Leparoux, R. Brossier, S. Operto, and O. Abraham, 2010, 2D quantitative imaging by elastic full waveform inversion: Application to a physical scale model: Presented at 16th European Meeting of Environmental and Engineering Geophysics.
- Brossier, R., 2011, Two-dimensional frequency-domain visco-elastic full waveform inversion: Parallel algorithms, optimization and performance: Computers & Geosciences, **37**, 444–455, doi: [10.1016/j.cageo.2010.09.013](https://doi.org/10.1016/j.cageo.2010.09.013).
- Brossier, R., S. Operto, and J. Virieux, 2009, Seismic imaging of complex onshore structures by two-dimensional elastic frequency-domain full-waveform inversion: Geophysics, **74**, no. 6, WCC105–WCC118, doi: [10.1190/1.3215771](https://doi.org/10.1190/1.3215771).

- Buehmann, J., and K. Holliger, 1998, Comparison of high-frequency seismic sources at the Grimsel Test Site, Central Alps, Switzerland: *Geophysics*, **63**, 1363–1370, doi: [10.1190/1.1444438](https://doi.org/10.1190/1.1444438).
- Cabrera, J., 2002, Evaluation of the 3D seismic high-resolution method at argillaceous Tournemire IRSN site: Presented at EUROSAFE 2002.
- Cabrera, J., P. Volant, C. Baker, W. Pettitt, and R. Young, 1999, Structural and geophysical investigations of the EDZ (Excavation Disturbed Zone) in indurated argillaceous media: The tunnel and the galleries of the IPSN Tournemire site (France): Presented at Vail Rocks, 37th U.S. Symposium on Rock Mechanics (USRMS).
- Cardarelli, E., C. Marrone, and L. Orlando, 2003, Evaluation of tunnel stability using integrated geophysical methods: *Journal of Applied Geophysics*, **52**, 93–102, doi: [10.1016/S0926-9851\(02\)00242-2](https://doi.org/10.1016/S0926-9851(02)00242-2).
- Constantin, J., 2002, Fracturation et paléocirculations de fluides dans les formations géologiques de faible perméabilité matricielle — Le cas des argilités de Tournemire (Aveyron, France): Ph.D. thesis, Université de Paris XI–Orsay.
- Cosma, C., and N. Enescu, 2001, Characterization of fractured rock in the vicinity of tunnels by the swept impact seismic technique: *International Journal of Rock Mechanics and Mining Sciences*, **38**, 815–821, doi: [10.1016/S1365-1609\(01\)00046-6](https://doi.org/10.1016/S1365-1609(01)00046-6).
- Côte, P., 1988, Tomographies sismiques en génie civil: Ph.D. thesis, Université de Grenoble.
- Gao, F., A. Levander, R. Pratt, C. Zelt, and G.-L. Fradelizio, 2007, Waveform tomography to a groundwater contamination site: Surface reflection data: *Geophysics*, **72**, no. 5, G45–G55, doi: [10.1190/1.2752744](https://doi.org/10.1190/1.2752744).
- Gélis, C., J. Cabrera, J.-D. Barnichon, I. Contrucci, P. Cote, D. Leparoux, and O. Magnin, 2010, Auscultation of underground works with seismic methods: Presented at Journées Nationales de Géotechnique et de Géologie de l'Ingenieur JNGG 2010.
- Gendzwil, D., and R. Brehm, 1993, High resolution seismic reflections in a potash mine: *Geophysics*, **58**, 741–748, doi: [10.1190/1.1443459](https://doi.org/10.1190/1.1443459).
- Gilbert, P., 1972, Iterative methods for the three dimensional reconstruction of an object from projections: *Journal of Theoretical Biology*, **36**, 105–117, doi: [10.1016/0022-5193\(72\)90180-4](https://doi.org/10.1016/0022-5193(72)90180-4).
- Gritto, R., V. Korneev, T. Daley, M. Feighner, E. Majer, and J. Peterson, 2004, Surface-to-tunnel seismic tomography studies at Yucca Mountain, Nevada: *Journal of Geophysical Research*, **109**, B03310, doi: [10.1029/2002JB002036](https://doi.org/10.1029/2002JB002036).
- Hedan, S., P. Cosenza, V. Valle, P. Dudoignon, A.-L. Fauchille, and J. Cabrera, 2012, Investigation of the damage induced by desiccation and heating of Tournemire argillite using digital image correlation: *International Journal of Rock Mechanics and Mining Sciences*, **51**, 64–75, doi: [10.1016/j.ijmms.2012.01.001](https://doi.org/10.1016/j.ijmms.2012.01.001).
- Inazaki, T., H. Ishahai, S. Kawamura, T. Kurahashi, and H. Hayashi, 1999, Stepwise application of underground seismic profiling for tunnel prediction ahead of the face: *The Leading Edge*, **18**, 1429–1431, doi: [10.1190/1.1438246](https://doi.org/10.1190/1.1438246).
- IPCC, 2005, IPCC special report on carbon dioxide capture and storage: Cambridge University Press.
- Jetschny, S., T. Bohlen, and D. De Nil, 2010, On the propagation characteristics of tunnel surface-waves for seismic prediction: *Geophysical Prospecting*, **58**, 245–256, doi: [10.1111/j.1365-2478.2009.00823.x](https://doi.org/10.1111/j.1365-2478.2009.00823.x).
- Jetschny, S., T. Bohlen, and A. Kurzmann, 2011, Seismic prediction of geological structures ahead of the tunnel using tunnel surface waves: *Geophysical Prospecting*, **59**, 934–946, doi: [10.1111/j.1365-2478.2011.00958.x](https://doi.org/10.1111/j.1365-2478.2011.00958.x).
- Kneib, G., A. Kassel, and K. Lorenz, 2000, Automatic seismic prediction ahead of the tunnel boring machine: *First Break*, **18**, 295–302, doi: [10.1046/j.1365-2397.2000.00079.x](https://doi.org/10.1046/j.1365-2397.2000.00079.x).
- Kruger, D., R. Groschup, and T. Dickmann, 2010, Integrated seismic 3D-processing for tunneling: Presented at 16th European Meeting of Environmental and Engineering Geophysics.
- Leparoux, D., P. Côte, C. Gélis, and J. C. Nunez, 2012, EDZ characterization with surface wave analysis: Experimental and numerical study for defining feasibility in the context of the Tournemire Platform (France): *Near Surface Geophysics*, **10**, 401–411, doi: [10.3997/1873-0604.2012033](https://doi.org/10.3997/1873-0604.2012033).
- Magnin, O., 2010, Technical report TERRASEIS-IRSN — Projet de recherche pour la detection des failles a faible decalage vertical dans les milieux argileux: Caracterisation de revolution des vitesses sismiques au passage de la faille principale: Technical report RD-SIS-10-30, TERRASEIS-IRSN.
- Magnin, O., and P. Côte, 2006, Essais de caracterisation de l'EDZ par sismique refraction tres haute resolution et test de sismique reflexion thr en galerie: Technical report RD- SIS-06-02, TERRASEIS-IRSN.
- Manukyan, E., H. Maurer, S. Marelli, S. Greenhalgh, and A. Green, 2012, Two-dimensional frequency-domain visco-elastic full waveform inversion: Parallel algorithms, optimization and performance: *Geophysics*, **77**, no. 6, EN73–EN83, doi: [10.1190/geo2011-0420.1](https://doi.org/10.1190/geo2011-0420.1).
- Marelli, S., H. Maurer, and E. Manukyan, 2012, Validity of the acoustic approximation in full-waveform seismic crosshole tomography: *Geophysics*, **77**, no. 3, R129–R139, doi: [10.1190/geo2011-0274.1](https://doi.org/10.1190/geo2011-0274.1).
- Matray, J.-M., S. Savoye, and J. Cabrera, 2007, Desaturation and structure relationships around drifts excavated in the well-compacted Tournemire's argillite (Aveyron, France): *Engineering Geology*, **90**, 1–16, doi: [10.1016/j.enggeo.2006.09.021](https://doi.org/10.1016/j.enggeo.2006.09.021).
- Maurer, H., and A. Green, 1997, Potential coordinate mislocations in cross-hole tomography: Results from the Grimsel Test Site, Switzerland: *Geophysics*, **62**, 1696–1709, doi: [10.1190/1.1444269](https://doi.org/10.1190/1.1444269).
- Menke, W., 1989, *Geophysical data analysis: discrete inverse theory*: Academic Press.
- Metivier, L., R. Brossier, J. Virieux, and S. Operto, 2013, Full waveform inversion and the truncated Newton method: *SIAM Journal on Scientific Computing*, **35**, B401–B437, doi: [10.1137/120877854](https://doi.org/10.1137/120877854).
- Nicollin, F., D. Gibert, P. Bossard, C. Nussbaum, and C. Guervilly, 2008, Seismic tomography of the Excavation Damaged Zone of the Gallery 04 in the Mont Terri Rock Laboratory: *Geophysical Journal International*, **172**, 226–239, doi: [10.1111/j.1365-246X.2007.03615.x](https://doi.org/10.1111/j.1365-246X.2007.03615.x).
- Nocedal, J., and S. Wright, 1999, *Numerical optimization*: Springer.
- Operto, S., J. Virieux, J.-X. Dessa, and G. Pascal, 2006, Crustal seismic imaging from multifold ocean bottom seismometer data by frequency domain full waveform tomography: Application to the Eastern Nankai trough: *Journal of Geophysical Research*, **111**, B09306, doi: [10.1029/2005JB003835](https://doi.org/10.1029/2005JB003835).
- Petronio, P., and F. Poletto, 2002, Seismic-while-drilling by using tunnel boring machine noise: *Geophysics*, **67**, 1798–1809, doi: [10.1190/1.1527080](https://doi.org/10.1190/1.1527080).
- Plessix, R.-E., 2006, A review of the adjoint-state method for computing the gradient of a functional with geophysical applications: *Geophysical Journal International*, **167**, 495–503, doi: [10.1111/j.1365-246X.2006.02978.x](https://doi.org/10.1111/j.1365-246X.2006.02978.x).
- Podvin, P., and I. Lecomte, 1991, Finite difference computation of travel-times in very contrasted velocity models: A massively parallel approach and its associated tools: *Geophysical Journal International*, **105**, 271–284, doi: [10.1111/j.1365-246X.1991.tb03461.x](https://doi.org/10.1111/j.1365-246X.1991.tb03461.x).
- Poletto, F., and P. Petronio, 2006, Seismic interferometry with a TBM source of transmitted and reflected waves: *Geophysics*, **71**, no. 4, SI85–SI93, doi: [10.1190/1.2213947](https://doi.org/10.1190/1.2213947).
- Pratt, R., 1999, Seismic waveform inversion in the frequency domain, part 1: Theory and verification in a physical scale model: *Geophysics*, **64**, 888–901, doi: [10.1190/1.1444597](https://doi.org/10.1190/1.1444597).
- Pratt, R., and R. Shipp, 1999, Seismic waveform inversion in the frequency domain, Part 2: Fault delineation in sediments using crosshole data: *Geophysics*, **64**, 902–914, doi: [10.1190/1.1444598](https://doi.org/10.1190/1.1444598).
- Pratt, R., and M. Worthington, 1990, Inverse theory applied to multi-source cross-hole tomography. I: Acoustic wave-equation method: *Geophysical Prospecting*, **38**, 287–310, doi: [10.1111/j.1365-2478.1990.tb01846.x](https://doi.org/10.1111/j.1365-2478.1990.tb01846.x).
- Ramambasoa, N., 2001, Etude du comportement hydromecanique des argillites: Ph.D. thesis, Ecole Polytechnique.
- Sattel, G., P. Frey, and R. Amberg, 1992, Prediction ahead of the tunnel face by seismic methods — Pilot project in Centovalli tunnel, Locarno, Switzerland: *First Break*, **10**, 19–25, doi: [10.3997/1365-2397.1992002](https://doi.org/10.3997/1365-2397.1992002).
- Schmidt, G., 1959, Results of underground seismic reflection investigations in the Siederite district of the Siegerland: *Geophysical Prospecting*, **7**, 287–290, doi: [10.1111/j.1365-2478.1959.tb01470.x](https://doi.org/10.1111/j.1365-2478.1959.tb01470.x).
- Shen, J., A. Leeds, M. Buddensiek, and G. Schuster, 2006, Early arrival waveform tomography on near-surface refraction data: *Geophysics*, **71**, no. 4, U47–U57, doi: [10.1190/1.2210969](https://doi.org/10.1190/1.2210969).
- Shen, X., 2010, Near-surface velocity estimation by weighted early-arrival waveform inversion: 80th Annual International Meeting, SEG, Expanded Abstracts, 1975–1979.
- Sirgue, L., and R. Pratt, 2004, Efficient waveform inversion and imaging: A strategy for selecting temporal frequencies: *Geophysics*, **69**, 231–248, doi: [10.1190/1.1649391](https://doi.org/10.1190/1.1649391).
- Song, Z., P. Williamson, and R. Pratt, 1995, Frequency-domain acoustic-wave modeling and inversion of crosshole data: Part 2 — Inversion method, synthetic and real-data results: *Geophysics*, **60**, 796–809, doi: [10.1190/1.1443818](https://doi.org/10.1190/1.1443818).
- Tarantola, A., 1984, Inversion of seismic reflection data in the acoustic approximation: *Geophysics*, **49**, 1259–1266, doi: [10.1190/1.1441754](https://doi.org/10.1190/1.1441754).
- Taylor, N., J. Merriam, and D. Gendzwil, 2001, The mining machine as a seismic source for in-seam reflection mapping: 71st Annual International Meeting, SEG, Expanded Abstracts, 1365–1368.
- Thomsen, L., 1986, Weak elastic anisotropy: *Geophysics*, **51**, 1954–1966, doi: [10.1190/1.1442051](https://doi.org/10.1190/1.1442051).
- Virieux, J., and S. Operto, 2009, An overview of full-waveform inversion in exploration geophysics: *Geophysics*, **74**, no. 6, WCC1–WCC26, doi: [10.1190/1.3238367](https://doi.org/10.1190/1.3238367).
- Zhu, Y., I. Tsvankin, P. Dewangan, and K. V. Wijk, 2007, Physical modeling and analysis of p-wave attenuation anisotropy in transversely isotropic media: *Geophysics*, **72**, no. 1, D1–D7, doi: [10.1190/1.2374797](https://doi.org/10.1190/1.2374797).
- Zinsner, B., P. Meynier, J. Cabrera, and P. Volant, 2002, Vitesse des ondes ultrasonores, soniques et sismiques dans les argilites du tunnel de Tournemire. Effet de l'anisotropie et de la fracturation naturelle: *Oil & Gas Science and Technology*, **57**, 341–353.